Polarimetric Remote Sensing of Land and Snow/Ice Covers with the Spaceborne Microwave Radiometer WindSat

von
M.Sc. Phys. Parag S. Narvekar

14. May 2007

Contents

Abstract

Measurements from spaceborne microwave radiometers, such as the Scanning Multichannel Microwave Radiometer (SMMR), the Special Sensor Microwave/Imager (SSM/I) and the Advanced Microwave Scanning Radiometer (AMSR), are found to be useful in estimating various earth surface geophysical quantities, e.g. soil moisture and vegetation characteristics over land, snow water equivalent for snow covers and sea ice concentration. All these instruments have measured only the vertical and horizontal polarization component of the brightness temperature (T_{B}). WindSat is the first spaceborne radiometer to provide fully polarimetric measurements of the earth's emission. It was launched by US Navy in February 2003. It determines the polarization state of the emission in the form of Stokes vector consisting of four components. The first two components are the typically measured vertical and horizontal TB. WindSat additionally determines the difference between $\pm 45°$ linearly polarized (3rd Stokes component) and left and right hand circular polarized radiation (4th Stokes component). The polarimetric radiometry is primarily used to estimate the sea surface wind speed and direction. So far little was known about the information content of the Stokes vector over vegetation, bare soil, snow and sea ice. This thesis explores the polarimetric signal observed by WindSat over land, the Antarctic ice sheet and Arctic sea ice.

Over land, it is shown that the polarimetric signal depends on the orientation of surface features such as sand dunes in deserts, and extended structures in agricultural fields. This dependency is validated over the test sites of the Taklamakan desert and the Helongjiang agriculture fields in China using correlative data collected by the Advanced Spaceborne Thermal Emission and Refection Radiometer (ASTER). The ASTER images from thermal infrared sensor of 90

meter resolution are used to identify the vegetation and desert surface structures. Over the Antarctic ice sheet, the findings show that the polarimetric signatures at higher frequencies (37 GHz) depend on snow surface features, such as sastrugi orientation and surface topography, whereas at the lower frequency (10.7 GHz) the signal additionally depend on snow properties such as grain size and density. This dependency is validated using the results from previously made scatterometer studies with European Space agency SCATterometer (ESCAT) and NASA SCATterometer (NSCAT), demonstrating the potential of polarimetric radiometers to estimate scattering and emission properties from the single instrument. Finally, the analysis of one year of the weekly averaged 3rd and 4th Stokes components of Arctic sea ice shows the highest anisotropic signal during a week of early summer (June 21-27). This was interpreted as a result of melting of the overlying snow due to which the penetration depth decreases making higher frequencies (37 GHz) sensitive to surface structure.

List of Publications

Parts of the works presented in this thesis have been published and presented at conferences.

Reviewed

Narvekar, Parag. .S., Jackson,T. J., Bindlish, R., Li Li, Heygster, G., and Gaiser, P., 2007: Observations of land surface passive polarimetry with the WindSat instrument. *IEEE Trans. Geosci. Rem. Sens.*, **45** 2019–2028.

Rao,K. S., Al Jassar, H. K., Narvekar,Parag. S., Shardul,N. B., Sabbah. I. and Daniel,V., 2006: An assessment of brightness temperature data quality of MSMR of IRS-P4 satellite. *International Journal of Remote Sensing*, **27**, 2, 277–292.

Narvekar,Parag. S., Heygster,G., Jackson, T. J., Macelloni,G., Bindlish, R. and Notholt,N., submitted: Passive polarimetric microwave signatures observed over Antarctica, *IEEE Trans. Geosci. Rem. Sens.*

Proceedings/Reports/Abstract

Narvekar,P. S., Heygster,G., Jackson T. J. and Bindlish,R., 2007: Polarimetric microwave emission from the snow surface, 4th Stokes component analysis. *proceedings IGARSS.*

Narvekar,P. S., Heygster,G., Jackson, T. J., Bindlish, R. and Li Li, 2006: Azimuthal variations in polarimetric microwave measurements observed over Dome C, Antarctica. *The international society of Optical Engineering (SPIE) proceedings*

Narvekar,P. S., Jackson,T. J., Bindlish, R. and Li Li, 2006: Observa-

tion of Land Surface Passive Polarimetry with WindSat. *Proceedings of MicroRad.*

Narvekar, P. S., Heygster, G., Tonboe, R., Jackson, T. J., and Bindlish, R., 2007: Analysis of WindSat Measured polarimetric microwave brightness temperature over sea ice. *Geophysical Research Abstract*, **9**, 06670.

Narvekar,P. S.,and Rao,K. S., 2004: Brightness temperature data analysis from Advance Microwave Scanning Radiometer (AMSR-E) for snow cover mapping. *Proceedings of International Symposium on snow monitoring and avalanche, India* (**Best paper award received**).

Narvekar, P. S., Rao, K. S. and Reddy,C. D., 2001: Estimation of atmospheric delay on SAR Interferometry. *Proceedings of Indian Society of Remote Sensing, India*, (**Best paper award received**).

Narvekar, P. S., Heygster, G. and Tonboe, R., 2008: Analysis of WindSat measured passive fully polarimetric measurements over Arctic sea ice. *Tech. Rep., IUP, University of Bremen. Final Report for Danish Met. Insititute, Denmark.*

1 Introduction

Microwave remote sensing has been found to be a useful tool in exploring, mapping and monitoring various earth surface geophysical parameters, e.g. soil moisture, surface temperature, vegetation water content, snow water equivalent and sea ice concentration. These parameters are major elements for weather prediction and global climate models (Ulaby et al,. 1981). Electromagnetic radiation at these wavelengths is only moderately affected by cloud cover and light rain and, therefore sensors operating at these wavelengths offer themselves for uninterrupted observations as needed in meteorology. Microwave remote sensing techniques can be divided into two major categories, active and passive ones. Active systems utilize radars, scatterometers and altimeters. These consist of a transmitter emitting microwave pulses and a receiver collecting the pulses reflected from the earth surface. The radar and scatterometer data are expressed as backscattering coefficients, defined as the ratio of the power received to the power transmitted (Ulaby et al., 1982). Passive sensors consist of only a receiver, called radiometer. Such sensors measure the natural, thermal emission emitted from the earth surface in the selected microwave band. The measured signal is expressed as a brightness temperature, which is, under the Rayleigh-Jeans approximation, equal o the physical temperature of a black body emitting the same thermal power as the observed target.

Demonstrated applications of the two techniques have been different. The backscattering coefficient generally provides more information about the structural properties, such as the land surface topography and sea wave orientation when compared with radiometers, and secondarily it also depends on the dielectric constant of the target illuminated by the transmitter (Ulaby et al., 1982). For mapping the

surface two types of radar are in use, the Synthetic Aperture Radar (SAR) and the real aperture radar or scatterometer. The SAR has the higher spatial resolution, and they have been used for retrieving earth surface geophysical parameters such as soil moisture, snow characteristics and sea ice properties. Due to the high power required to generate the signal, most SARs are operated with a low duty cycle. In contrast, the real aperture radars (scatterometers) typically provide data continuously with higher temporal resolution but at lower spatial resolution. They have primarily been developed to retrieve the sea surface wind speed and direction, parameters, which are crucial for climate and weather prediction models (Gaiser et al., 2002).

Unlike radars, the signal of a radiometer primarily depends on the earth surface thermal and dielectric properties. Moreover, as the radiometer is a passive instrument not requiring a transmitter the power to operate such sensors is low. Over the last two decades, due to the use of larger antenna ,the spatial resolution has been improved, e.g. for the C-Band ($\sim$7 GHz) from 150 km for the Scanning Multichannel Microwave Radiometer (SMMR) launched in 1978, to 60 km for the Advanced Microwave Scanning Radiometer (AMSR-E) launched in 2002. This improvement in resolution has resulted in greater use of the data in applications such as regional scale weather prediction and mapping land surface features. Unlike as for remote sensing at visible or thermal wavelengths the polarization of microwave radiation carries relevant geophysical information. Traditionally, two polarizations are considered, vertical and horizontal. The horizontally polarized radiation is that in which the electric field vector of the waves oscillates in the plane parallel to the earth surface. For the vertically polarized radiation the waves oscillate in the plane perpendicular to the horizontal polarization. However, the complete description of the partially polarized radiation comprises four components, together called Stokes vector (Ulaby et al., 1982; Tsang et al., 1985). The first two are the vertical and horizontal polarized emissions, measured in terms of brightness temperatures, given as T_v and T_h, respectively. The other two components provide measures of correlation between the first two called as 3rd and 4th Stokes components, and are given as U and V and together denoted as higher Stokes components. Frequently the

natural emission is incoherent. In those cases, the U and V Stokes components are zero.

Specular water surfaces show partially polarized emission, i.e. different values for T_v and T_h. Wind roughening reduces this difference depending on the extent of roughness. This is useful in estimating the wind direction and speed. The magnitude of the difference is also sensitive to salinity and temperature, since T_v and T_h has primary dependency on dielectric and thermal properties. The U and V Stokes primarily depends on earth surface geometric structural properties and therefore are the better indicator of roughness effect. The roughness generated in the form of waves, due to surface winds, is periodic. The directivity of sea waves in a particular direction gives rise to nonzero higher Stokes components.

In order to take advantage of the information available in the polarization so called polarimetric radiometers were developed measuring simultaneously all four Stokes parameters. Ground based experiments observing periodic surfaces using a fully polarimetric radiometer have shown that the polarimetric emission is a function of the magnitude, the orientation and the periodicity (Nghiem et al., 1991) of the surface structure. In order to verify this over large areas, airborne polarimetric radiometers were used over wind generated sea surfaces and a methodology for sea surface wind vector retrievals was developed. However, little attention was given to the polarimetric response from other targets such as land, ice sheets and sea ice.

WindSat is the first spaceborne fully polarimetric radiometer. It was launched with the primary objective of sea surface wind vector retrievals from space. WindSat is an experimental mission by the United States Navy in collaboration with the National Polar orbiting Operational Satellite Systems (NPOESS) office. It was launched in February 2003 and in addition serves as risk reduction mission for the forthcoming instrument Conical Scanning Microwave Imager/Sounder (CMIS) of NPOESS (Gaiser et al., 2004). WindSat acquires data covering the full globe, while polar orbiting. This has created an opportunity to investigate what new information is present in the U and V components over land, glaciers and sea ice.

From the sea surface investigations, it has been shown that the U

and V primarily depend on the orientation of the sea waves. The initial investigations of polarimetric signatures over sea surfaces have utilized the geometric optics methods (Gasiewski and Kunkee, 1994). In this method, only large-scale gravity waves were considered as tilted facets, and modeled using the slope distributions in the upwind and crosswind direction. However, further studies showed that the small-scale waves are more sensitive to surface winds (Irisov et al., 1992). Therefore two scale models were developed to separately quantify the effects from the larger and smaller scale roughness with respect to the measured wavelengths (Yueh et al., 1994). Observations with a fully polarimetric airborne radiometer (WINDRAD) showed the importance of the look angle (azimuth angle) in polarimetric remote sensing (Yueh, 1997).

Chapter 2 discusses the theoretical basis of polarimetric remote sensing of the sea surface. The sea surface has been studied extensively and is used in the present study for making necessary conclusions for the other targets based on sea surface algorithms. Because of the importance of the azimuth angle in the polarimetric technique, it was necessary to investigate the bias associated with the WindSat look angle. The data quality check and the instrument scan angle selection were done based upon an external calibration target as discussed in Chapter 3.

For land surfaces, T_v and T_h are utilized in retrieving information such as large-scale soil moisture. A limitation of these retrievals is that often more parameters need to be determined than there are independent observations (an under determined system). Additional parameters of interest include multiple scales of roughness and more or less heterogeneous vegetation. Accurate information of these parameters are expected to improve accuracy of the present soil moisture algorithms. In Chapter 4 , WindSat data over large homogenous land surfaces with known surface topography and geophysical characteristics are investigated to explore the sensitivity of higher Stokes component on vegetation and soil surface roughness.

The polarimetric analysis of the Antarctic ice sheet is carried out in Chapter 5. The Antarctic ice sheet plays an important role in the global climate, e.g. as a region of low absorption of solar radiation. An initial analysis was carried out over several test sites, such as Dome C,

Wilkes Land, Terre Adelia and Queen Mary Land, which were studied previously with scatterometers (Long and Drinkwater, 2000). U and V signals of higher magnitude than over sea and land surfaces were observed. The result is then compared with the surface topography and scatterometer derived orientation of snow surface structures. In the next step the analyses is extrapolated over the entire Antarctic continent.

Chapter 6 is devoted to the quantitative analysis of the U and V signals of Arctic sea ice. Seven-day averages of U and V maps of the entire year 2003 were prepared. The Azimuthal dependency of U and V are taken into account by averaging the data over $90°$ intervals of azimuth angle. An anisotropic U signal has been observed at 37 GHz during early summer melting. The exact cause of this signal is not yet known. There are various geophysical processes takes place over the surface of the sea ice during early melting period. This is a topic of an ongoing research activity. Finally in Chapter 7 the results over the diverse targets land surface; bare soils and vegetated areas, Antarctic ice sheet and the Arctic sea ice is revised. and the thesis ends with an outlook.

2 Theoretical Background

The electromagnetic radiation consist of two components, the electric field $\boldsymbol{E}$ and the magnetic field $\boldsymbol{B}$. They are orthogonal (perpendicular) to each other, and mutually orthogonal to the direction of propagation, which is specified by a vector quantity $\boldsymbol{S}$ know as Poynting vector given as

$$\boldsymbol{S} = \boldsymbol{E} \times \boldsymbol{B} \tag{2.1}$$

The electric field is considered for representation of wave characteristics. In microwave remote sensing one has to always deal with the polarization components of the backscattered or emitted electric field from the Earth's surface and atmosphere. The polarization of an electromagnetic wave is referred to the direction of oscillation of the electric field of a wave with respect to the propagation direction. The electric field in the far field regime propagating in the direction, say $\boldsymbol{r}$, is primarily decomposed in to vertical and horizontal components. The microwave sensor systems operating at vertical and horizontal polarizations are called dual polarized systems. The different types of Earth's surface and their characteristics have been extensively investigated using horizontally and vertically polarized measurements. However, for the mediums with directional features, such as sea waves which are periodic in the direction of the surface winds, the additional polarimetric components may be used to characterize the target. The technique that utilize additional polarization components than vertical and horizontal is known as fully polarimetric microwave remote sensing.
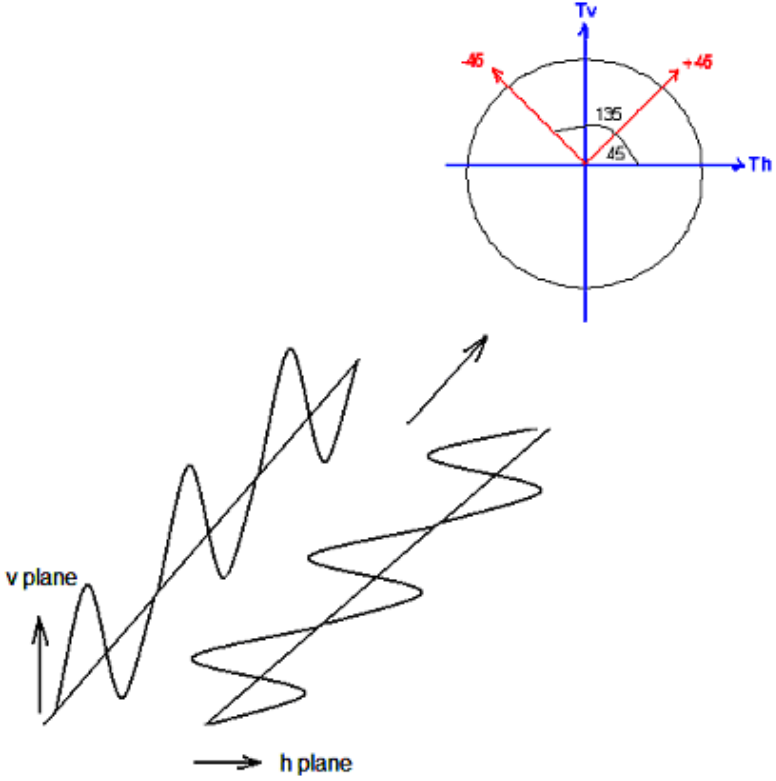
Figure 2.1: The vertical (v) and horizontal (h) Polarized waves.

2.1 Physical concept of polarization

For a horizontally polarized wave, the electric field component is parallel to the earth surface and perpendicular to the direction of propagation. The vertically polarized field is perpendicular to the plane formed by the propagation direction and the direction of the oscillation of the horizontally polarized electric field. Figure 2.1 depicts the propagation of a vertically and horizontally polarized sinusoidal wave. These waves can be represented in terms of the electric field vector as

$$\boldsymbol{E} = E_{0,h} cos(kr - \omega t)\boldsymbol{h} \tag{2.2}$$

where $E_{0,h}$ is the electric field component in h plane, k is the wave number and ω is the angular velocity and t is the time . The h can be replaced by v in the above equation to represent an wave oscillating in v plane with amplitude $E_{0,v}$. The amplitude E_0 is the strength of the electric field in the plane under consideration (i.e. h or v). In fully polarimetric microwave radiometers, the information about the polarization state of emission more than that provided by h and v is necessary for characterization of the target. These include the measurements in the $+45°$ and $-45°$ plane and the left and right circular polarizations. The $45°$ polarized wave is plane polarized, similar to that of h or v but oscillating at the angle of $-45°$ or $+45°$ to the plane of horizontal and vertical as shown in Figure 2.1. The circularly polarized wave can be generated using the combination of two plane polarized orthogonal waves with equal amplitude and $\pi/2$ phase shift between them. This mechanism is illustrated in Figure 2.2. The resultant of these two waves is a circularly polarized wave as illustrated in part B of Figure 2.2. In a circularly polarized wave, the vector rotates about the direction of propagation at the frequency of the light wave, i.e. one revolution per period of the wave. The circularly polarized wave shown above is left handed circularly polarized, since the resultant electric field rotates anticlockwise with respect to direction of propagation as shown in part C of the figure. Similarly, the right handed circularly polarized wave can be generated by introducing a phase shift of $-\pi/2$ on vertical polarized wave in above figure.

In the simplified mathematical format this can be represented as

$$\boldsymbol{E_{circ}} = E_0[cos(kr - \omega t)\boldsymbol{h} \pm sin(kr - \omega t)\boldsymbol{v}] \tag{2.3}$$

Above equations can also be written by applying the phase shift to a horizontally polarized wave instead of vertical. Secondly, the equation will also hold for any other plane polarized channels which are orthogonal to each other. For example, the shift between the $-45°$ and $+45°$ channels is used in the WindSat instrument for circular polarization measurements.

In active and passive microwave polarimetry the area under consideration is studied based on the polarized microwave radiations emitted
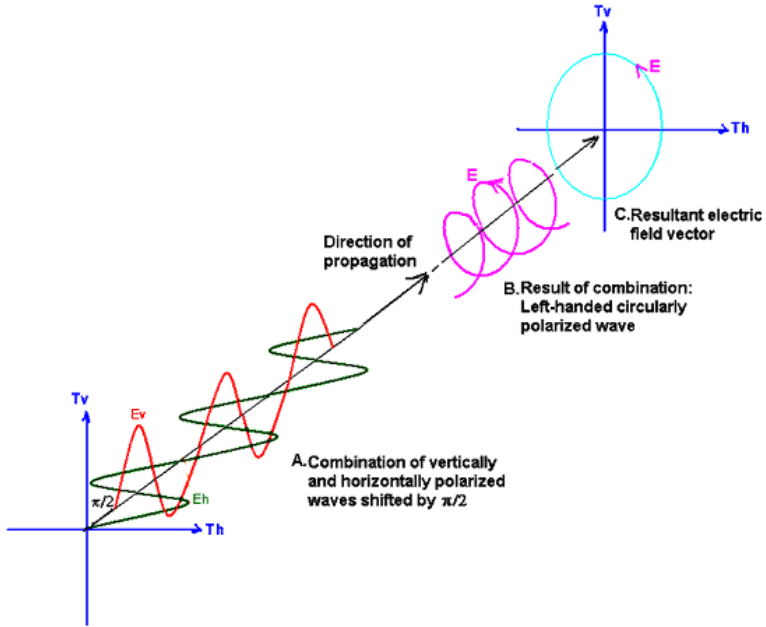
Figure 2.2: Formation of the circularly polarized wave from vertical and horizontal waves by introducing phase shift of $\pi/2$

and scattered from it. More work has been done in active polarimetric microwave remote sensing in land surface applications (Ulaby et al., 1986; Fung, 1994; Oh et al., 1992; Dubois et al., 1995) as compared to the passive polarimetric microwave remote sensing. The polarimetric emissions were extensively studied in radio astronomy (Hamaker et al., 1996). In remote sensing of the earth surface, till the launch of WindSat in 2003, the passive polarimetry was solely related to sea surface applications, such as wind speed and direction retrievals (Yueh et al., 1994). Very little was known about the land and snow surfaces, due to the lack of passive polarimetric observations. The present work investigates the passive polarimetry for the land and snow/ice surface. In order to develop background knowledge, the sea surface theoretical understanding is extended over land and snow surface. The sea surface theories in the use of sea surface application include the formulation used in the active microwave remote sensing.

2.2 Backscatter concept for active sensors

In an active system, the antenna transmits and receives back the scattered microwave pulses in vertical and/or horizontal polarization. The data is collected in the form of backscatter coefficient, which is a ratio of power received to the power transmitted (Ulaby et al., 1982; Tsang et al., 1985). If both the transmitted and received signals are horizontally/vertically polarized (h or v), the signal is said to be of hh or vv polarized. If the transmitted signal is horizontally polarized and the received signal is vertically polarized then the signal is said to be hv polarized and vice-versa. The co-polarization signals (hh and vv) and cross-polarization signals (hv and vh) along with the phase information between them constitute a fully polarimetric active observation. Active polarimetry is mainly useful in studies and applications associated with Earth's surface structure, such as mapping the topography. The radar cross section per unit area σ^0 also called scattering coefficient is defined as

$$\sigma^0 = \frac{\langle \sigma \rangle}{A_0} = \frac{4\pi R_r^2}{A_0} \frac{\langle |\boldsymbol{E^s}|^2 \rangle}{|\boldsymbol{E^i}|^2}. \tag{2.4}$$

Here, A_0 is the area illuminated by radar, R_r is size of the receiveing antenna and $\boldsymbol{E^s}$ and $\boldsymbol{E^i}$ are the electric field intensities of recieved and emitted signals. The scattering coefficient is a dimensionless quantity. It also depends on the polarization states of the emitted and received signals (Ulaby, 1982, Fung, 1994). Suppose p denotes the polarization of the emitted signal and q denotes polarization of the received one, then in terms of polarization the scattering cross section can be represented as

$$\sigma_{qp} = 4\pi R^2 \frac{|\boldsymbol{E_{qp}^s}|^2}{|\boldsymbol{E_{qp}^i}|^2} \tag{2.5}$$

and the scattering coefficient per unit area given in Equation (2.4) can be written as

$$\sigma_{qp}^0 = \frac{\langle \sigma_{qp} \rangle}{A_0} = \frac{4\pi R_r^2}{A_0} \frac{\langle |\boldsymbol{E_{qp}^s}|^2 \rangle}{|\boldsymbol{E_{qp}^i}|^2} \tag{2.6}$$

The Equations (2.5)and (2.6) represent the polarizations in terms of power equations. This formulation of different combinations of the scattering coefficient is used in the theory of passive polarimetric application, such as wind speed retrievals. The relationship between active and passive polarimetry is discussed in the next section.

2.3 Stokes vector in passive polarimetry

The potential of the horizontal and vertical brightness temperatures in the earth surface geophysical parameter retrievals, such as soil moisture (Jackson and Shmuggi, 1993) and snow water equivalent (Kunzi et al., 1976), are well known. The fully passive polarimetric microwave radiometers make use of the Stokes vector for the representation of the polarization state of naturally emitted radiations from the earth's surface. The Stokes vector consists of four components that define the polarization state of a electromagnetic wave. The Stokes components for completely polarized radiation are discussed in Tsang et al.(1985). In passive remote sensing, the natural radiations received by radiometers are the sum of statistically independent waves having the same averaged frequency and different polarizations and phase difference uniformly distributed over 0-2π. For periodic surfaces the radiations becomes partially polarized and its polarimetric state can be explained based on the Stokes vector (Tsang et al., 1985). For partially polarized radiations it is defined by the time averaging procedure given as

$$
I = \begin{bmatrix} T_v \\ T_h \\ U \\ V \end{bmatrix} = \frac{1}{\eta} \begin{bmatrix} \langle E_v E_v^* \rangle \\ \langle E_h E_h^* \rangle \\ 2Re \langle E_v E_h^* \rangle \\ 2Im \langle E_v E_h^* \rangle \end{bmatrix}
\tag{2.7}
$$

where, η impedance of the medium and $\langle\,\rangle$ denotes the time average. In Equation (2.7) U and V are referred as the 3rd and 4th Stokes components. T_v and T_h correspond to ensemble time average of the electric field and their complex conjugates in vertical and horizontal polarization planes, respectively. U and V correspond to the real and

imaginary parts of combination of ensemble average over vertical and complex conjugate of horizontal electric field vector, respectively. The Stokes vector presented in equation (2.7) is calculated from the h and v polarized channels. Also in active polarimetry only h and v channels are utilized in estimating polarization states as discussed in Section 2.2. The airborne radiometers, such as WINDRAD of NASA has made use of v and h polarized channels for calculating the Stokes vector (Yueh et al., 1999). However, in passive polarimetry it is possible to make the use of additional measurements, discussed in Section 2.1, for the calculation of Stokes vector. There, the polarization state of radiations is measured using $+45°$ and $-45°$ plane polarized, and left and right handed circularly polarized channels. These measurements form the Stokes vector that can be given as

$$I = \begin{bmatrix} T_v \\ T_h \\ U \\ V \end{bmatrix} = \begin{bmatrix} T_v \\ T_h \\ T_{45} - T_{+45} \\ T_{lc} - T_{rc} \end{bmatrix} \qquad (2.8)$$

WindSat makes use of this technique to calculate the Stokes vector given by equation (2.8). The 3rd and 4th Stokes parameters give a measure of correlation between vertically and horizontally polarized waves that are emitted from the periodic or rougher earths surface. Till date the research in passive polarimetry is mainly focused on periodic features of the earth's surface e.g. ocean wave and is used for calculating wind speed and direction over sea surface (Yueh, 1997; Yueh, et al., 1999; Piepmeier, et al., 2001, Gaiser, et al., 2004).

2.4 Relationship between bistatic scattering coefficient and Stokes vector

T_v and T_h are functions of temperature and dielectric constant and secondarily depend upon the roughness and geometric properties of

the medium. The brightness temperature at vertical or horizontal polarizations can be written as,

$$T_{Bp} = e_p T_s \qquad (2.9)$$

where p corresponds to v or h, T_s is the earth surface temperature and e is the emissivity which can be written as

$$e_p = 1 - r_p \qquad (2.10)$$

The formulation of the reflectivity,r typically utilized over land surface, can be written using the Fresnel's expression for specular surfaces

$$r_v = \left| \frac{\varepsilon_r cos\theta - \sqrt{\varepsilon_r - sin^2\theta}}{\varepsilon_r cos\theta + \sqrt{\varepsilon_r - sin^2\theta}} \right|^2 \qquad (2.11)$$

and

$$r_h = \left| \frac{cos\theta - \sqrt{\varepsilon_r - sin^2\theta}}{cos\theta + \sqrt{\varepsilon_r - sin^2\theta}} \right|^2 \qquad (2.12)$$

where θ is the incidence angle and ε is the complex dielectric constant. This makes thermal and dielectric properties of the target to play a critical role in the brightness temperature measured at these two polarizations (the first two Stokes components). On the other hand, U and V primarily depend on the structural properties of the target and secondarily depend on the dielectric properties. Similar is the case for the backscatter coefficient measured in active microwave remote sensing. This is the main reason for the application of the active polarimetric theory in the passive polarimetry. However, while relating the passive and active concepts some approximations needs to be considered.

Tsang et al.(1985) derived the reciprocity relation for the inhomogeneous and anisotropic surface of active backscattering coefficient. This understanding is then utilized in Kirchhoff's Law for relating reflectivity to active backscattering coefficient. Consider Figure 2.3 showing
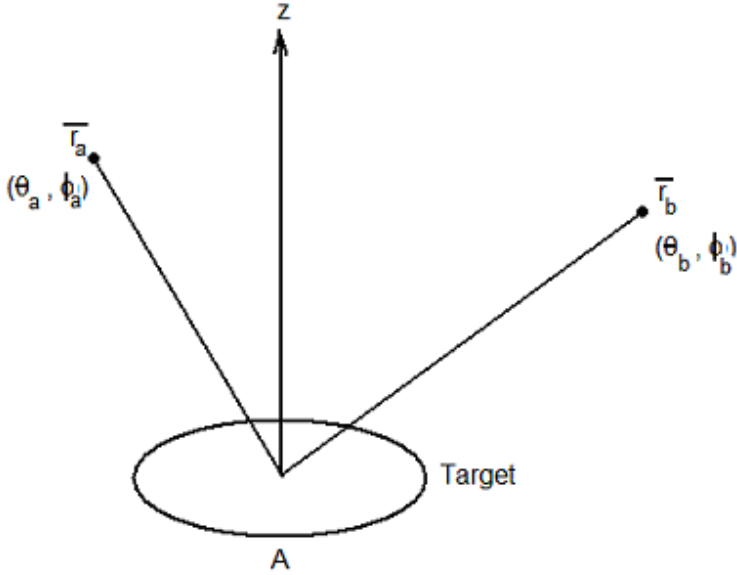
Figure 2.3: Geometry of transmitting and receiving signal from points r_a and r_b for explanation of reciprocity theorem

two points one at r_a and other at r_b each at different incidence and azimuth angles. Then from the reciprocity relation we have,

$$cos\theta_a \gamma_{pq}(\theta_b, \varphi_b; \theta_a, \varphi_a) = cos\theta_b \gamma_{pq}(\theta_a, \varphi_a; \theta_b, \varphi_b) \tag{2.13}$$

where p and q corresponds to the polarization of the incidence and reflected radiation. γ_{pq}, is the bistatic scattering coefficient and in terms of the earlier defined scattering cross section, Equation (2.6), can be written as,

$$\sigma_{pq} = cos\theta_i \cdot \gamma_{pq} \tag{2.14}$$

where θ_i was the incident angle of radar emitted radiation. Therefore, the wave incident from a point at r_a and reflected signal measured at r_b is related to the wave incidence from r_b and measured at r_a.

The Equation (2.13) takes in to account the variation of the incidence angle in the look range of radar. Kirchhoff's law describes the relation between the emissivity and absorptivity of the body, i.e. the relation between the energy absorbed to the energy emitted. The emission of the body also depends upon the temperature. In thermal equilibrium the energy absorbed should be equal to energy emitted. Unlike radars, there is no energy emitted out from the radiometer and it measures only the natural emission of the Earth's surface emitted into its direction. If the medium is considered to be in thermal equilibrium then using the reciprocity theorem, the emissivity can be defined using the bistatic scattering coefficient of the active theory as given in the following Equation (2.14).

$$|R_q(\theta_i)|^2 = \frac{1}{4\pi} \sum \int d\Omega_s \gamma_{pq}(\theta_s, \varphi_s; \theta_i, \varphi_i) \tag{2.15}$$

The detail derivation and explanation can be found in Tsang et al.(1985). The reflectivity Equation (2.15) is used to define the polarimetric brightness temperature dependency on the structural properties of the target.

2.5 Symmetry properties of polarimetric brightness temperature and periodic surfaces

To explain the symmetry properties of the electric field Yueh et al.(1994) defined a reflection operator. In that study it was shown that the Maxwell's equations remain invariant for the intensity of the radiations (electric fields) obtained, if the reflection operator operated on the plane of symmetry. This is depicted in Figure 2.4.

However the reflection operatore R changes the sign of the y vector component of the image field. Based on this property of the opera-

Reflection
Plane

$\overline{A} = (A_x, A_y, A_z)$ z $R(\overline{A}) = (A_x, -A_y, A_z)$

a $R(a) = a$

$\overline{r} = (x, y, z)$ $R(\overline{r}) = (x, -y, z)$
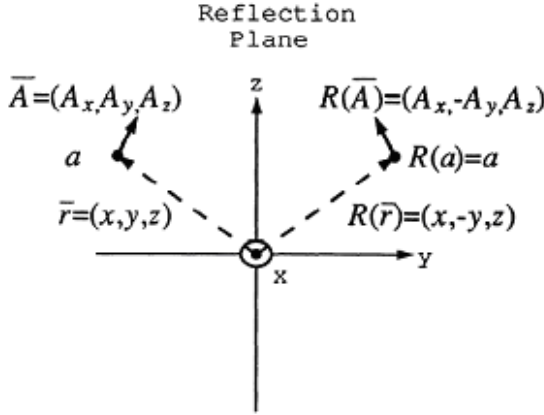
x y

Figure 2.4: The relation between the original field and the image field, (adopted from Yeuh et al, 1994)

tor R, Tsang et al.(1985) established the symmetry properties of the components of the Stokes vector:

$$T_v(\theta, \varphi) = T_v(\theta, -\varphi)$$

$$T_h(\theta, \varphi) = T_h(\theta, -\varphi)$$

$$U(\theta, \varphi) = -U(\theta, -\varphi) \qquad (2.16)$$

$$V(\theta, \varphi) = -V(\theta, -\varphi)$$

From Equation(2.16) it is apparent that T_v and T_h of the reflection symmetric media are even functions of φ, while the 3rd and 4th Stokes components are odd functions. Equation (2.16) forms a very important result and form the basis for U and V application over sea surface.

Winds gives rise to sea surface waves that are symmetric with respect to the wind direction. In the sea surface theory, instead of azimuth angle so called the relative azimuth angle φ is used. It is the

difference between radiometer look angle φ_r and wind direction φ_w

$$\varphi = \varphi_w - \varphi_r. \tag{2.17}$$

φ_w is measured with respect to geographic north. The relative azimuth angle is sometimes referred to as relative wind direction (Yueh, 1997). Therefore, for a reflection symmetric surface of sea waves, the Stokes parameters can be expressed as even and odd functions of the relative azimuth angle. This symmetric nature of the wind generated sea surface further allows the Stokes vectors to be expressed as second harmonic sine or cosine series of φ as presented in following equations (Yueh, 1997)

$$T_v = T_{v0} + T_{v1}cos(\varphi) + T_{v2}cos2(\varphi) \tag{2.18}$$

$$T_h = T_{h0} + T_{h1}cos(\varphi) + T_{h2}cos2(\varphi) \tag{2.19}$$

$$U = U_1 sin(\varphi) + U_2 sin2(\varphi) \tag{2.20}$$

$$V = V_1 sin(\varphi) + V_2 sin2(\varphi). \tag{2.21}$$

Here, the first harmonic accounts for the upwind and downwind asymmetry, and the second harmonic account for the upwind and cross wind asymmetry (Yueh, 1997). The coefficients in these equations are functions of instrument parameters, wind speed and other sea surface parameters such as salinity and surface temperature. Higher harmonic components must be zero because they would violate the symmetry properties.

2.6 Overview of some methodologies used in sea wind vector retirevals

Different methods have been investigated to retrieve the wind vector from polarimetric observations. These methods deal with extracting

wind information present in the first and second harmonic coefficients if the ocean salinity and surface temperature are known. Some of the analytical and numerical methods includes extended boundary condition method (EBCM), Methods of Momentum (MoM), Small Slope Approximation method (SSA) and Two Scale Method. In the applications over the sea surface, only the two scale method is shown to have a higher reliability (Yueh et al, 2006). An example is the approach followed by Yueh(1997) and Yueh(2006) for airborne observations of WINDRAD and for the spaceborne observations of WindSat, respectively. In this method the sea surface roughness is defined on two scales; the large scale roughness (waves larger then the measured microwave signal) and the small scale roughness (waves smaller then the measured microwave signal, known as capillary waves). The large scale roughness is modelled using geometric optics, where the large scale waves are treated as tilted facets and their slope distribution in along wind and cross wind direction is considered for the generation of the polarized microwave emission. Isrove(1991) showed that the small scale waves are more sensitive towards the wind speed and direction. The effect from these small scale waves are usually modelled considering backscattering coefficient theory. In the approach provided by Yueh(1997), the Stokes vector given in Equation (2.7) is given as a sum of two matrices corresponding to coherent and incoherent radiations. Usually, the higher order scattering, usually 2nd order, produce the coherent signal.

The present work is solely related to the passive polarimetric responses observed over land and snow/ice. For such targets, unlike sea surface, the volume scattering also plays a critical role for the generation of the U and V components. Understanding developed in this section will be helpful in the development of methodology for the application of U and V over the land and snow/ice surface.

3 Instrumentation and Data

WindSat is the first spaceborne fully polarimetric microwave radiometer acquiring data over ocean, land and snow/ice surfaces while polar orbiting. It was launched on January 6, 2003 and is sponsored by the U.S. Department of Defense (DoD) Space Test Program (STP), the U.S. Navy and the National Polar-Orbiting Operational Environmental Satellite System (NPOESS) integrated program office. It was developed to test the possibility of the sea surface wind speed and direction estimation from space. The mission also provides so called risk reduction data for an instrument called the Conically-scanned Microwave Imager Sounder (CMIS) that will be part of the National Polar-Orbiting Operational Environmental Satellite System (NPOESS).

WindSat was launched on the Coriolis spacecraft, fully redundant three-axis stabilized spacecraft (nadir pointing). The overall dimensions are: 4.69 m height (without solar array), 1.34 m diameter. Figure 3.1 shows the photograph of the WindSat and the schematic diagram of spacecraft and feed horns of different frequencies and polarization. Key features of the Coriolis spacecraft design include:

• Extremely low levels of electromagnetic interference for compatibility with the ultra-sensitive WindSat radiometer (e.g., radiated emissions are <6.5 dB μV/m at 6.8 GHz).

• System architecture to support the 31 rpm yaw spin of WindSat's rotating assembly, while providing power plus precise attitude knowledge and control.

The nominal orbit parameters for CORIOLIS are defined as;

• 840 km circular,

• 98.7 degree inclination,

• Sun synchronous,

- Revisit time of 8 days,
- Local time of ascending node (LTAN) of 6 PM,
- Westward-shifting longitude of the ascending node by 138 km daily.
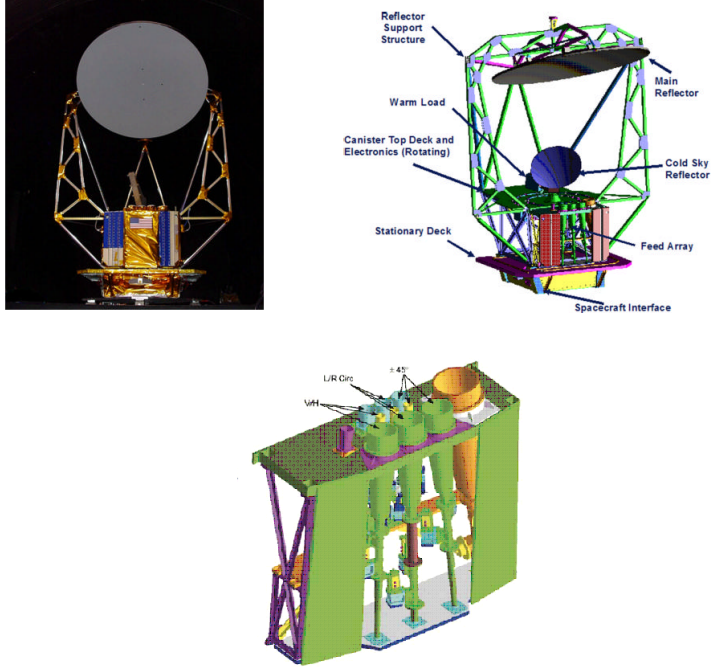

Figure 3.1: WindSat instrument and its schematic diagram (adopted from NRL doc. 2005).

WindSat operates at five frequencies 6.8, 10.7, 18.7, 23.8 and 37 GHz. The 6.8 and 23.8 are dual polarized channels, i.e. they are operated only at vertical and horizontal polarization. The 10.7, 18.7 and 37 are the fully polarimetric channels, i.e the brightness temperature is measured at +45°, -45°, left circular and right circular polarization in addition to vertical and horizontal. The different color feedhorns in Figure 3.1 correspond to different frequencies. For 10.7, 18.7 and 37 GHz there are three fedhorns which make separate measurements for

h and v, $+45°$ and $-45°$ plane polarized, and left circular and right circular polarized measurements. The data is provided in the form of the Stokes vector, discussed in Chapter 2, given as

$$
I = \begin{bmatrix} T_v \\ T_h \\ U \\ V \end{bmatrix} = \begin{bmatrix} T_v \\ T_h \\ T_{45} - T_{+45} \\ T_{lc} - T_{rc} \end{bmatrix}.
\tag{3.1}
$$

Table 3.1 WindSat instrument specifications

Freq. (GHz)	Pol.	Inc. Ang.(°)	F.print (km)	Fore/Aft Swath (km)
6.8	v, h	53.5	40 x 60	1025/350
10.7	v, h, U, V	49.9	25 x 38	1025/350
18.7	v, h, U, V	55.3	16 x 27	1025/350
23.8	v, h	53.0	12 x 20	1025/350
37	v, h, U, V	53.0	8 x 13	1025/350

Table 3.1 provides the specification of each channel in terms of incidence angle, polarization and resolution. The incidence angle slightly differs for each frequencies. For the data acquisition, only a limited range of scan angle in fore and aft swath are considered. This is since for some scan angles the radiometer is under warm and cold space calibrations. Moreover, data acquisition at some of the scan angles are also restricted due to the bias associated with the measurements, discussed in Section 3.2. Figure 3.2 shows the position of the cold and the hot calibration loads with respect to the instrument scan angle.

3.1 Data description

WindSat produces approximately 200 Mbytes of data per orbit, or 2.8 GB/day. The Ground Data Processing Software (GDPS) consists of four main processors:
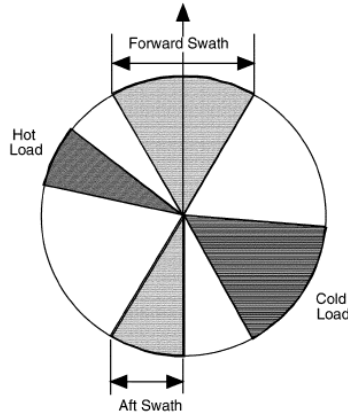
1) Raw Data Record Processor (RDRP);

Figure 3.2: The WindSat data acquisition geometry, location of cold and hot calibration loads (adopted from Jones, et al 2006).

a) receives the WindSat data stream, including receiver, calibration, housekeeping and spacecraft attitude data.
b) decodes, unpacks, reformats and merges these data.

2) Temperature Data Record Processor (TDRP);
a) calibrates the raw counts into radiances using the calibration target measurements and the sensor constants file.
b) geolocates each channel, using the scan angle, spacecraft attitude and ephemeris and antenna pointing offset.
c) calculates various antenna pointing parameters (earth incidence angle, polarization rotation angle, surface compass azimuth angle) using the spacecraft attitude and ephemeris along with pre-launch antenna alignment data.

3) Sensor Data Record Processor (SDRP);
a) collocate data pixels within frequency bands. At this point, one has all six polarizations for a polarimetric channel spatially collocated.
b) forms the third and fourth elements (U and V) of the Stokes vectors by taking the difference of the appropriate polarization pairs.
c) apply the antenna pattern correction (APC) using cross-polarization

correction (using h and v polarized measurements and feed spillover efficiencies, and correct for the PRA.

d) for each frequency, re-sample all channels to a common location defined by 37 GHz V/H channels.

e) Average antenna beams to yield collocated pixels at a common resolution.

4) Environmental Data Record Processor (EDRP) or the L2 Processor;

a) receives calibrated, geolocated, co-registered WindSat Stokes parameters at 10.7, 18.7 and 37 GHz, and the vertical and horizontally polarized brightness temperatures at 6.8 and 23.8 GHz.

b) Retrieves geophysical parameters which currently includes ocean surface wind speed and direction, columnar water vapor, columnar cloud liquid water, sea surface temperature, and rain rate over the ocean.

3.2 Quality check and filtering

For the current investigation, the sensor data record (SDR) version 1.9 available from June 2003 to January 2005 was used. In microwave remote sensing of the Earth's surface, incidence angle plays a critical role in the magnitude of T_{B} (Ulaby et al., 1982). Studies have shown a dependency of polarimetric measurements on azimuth angle in addition to incidence angle (Yueh et al., 1993; Yueh, 1997). For WindSat, the incidence angle is fixed for each channel (Table 3.1) but azimuth look angle will vary.

Azimuth look geometry involves two components, the scan angle and the azimuth angle. The scan angle (φ_{scan}) is the radiometer look angle with respect to the flight direction, where 0° lies on the ground track with positive values to the left and negative to the right. The azimuth angle is the radiometer look angle (φ_{rad}) with respect to geographic north and varies from 0° to 360°. A simplified WindSat data acquisition geometry for a descending pass is shown in Figure 3.3. Even though the instrument is conically scanning, only a lim-
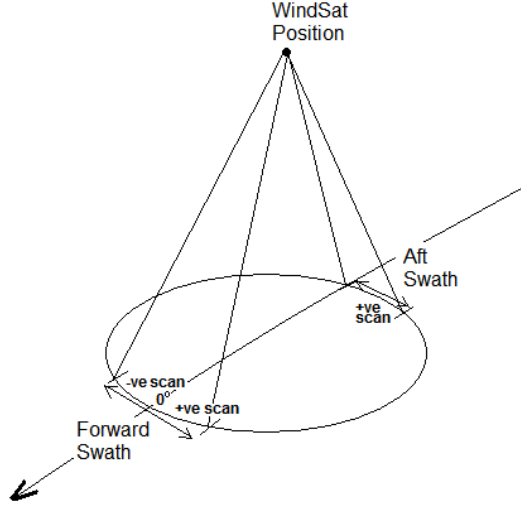
Figure 3.3: WindSat data acquisition geometry.

ited range of data in the forward swath and the aft swath is actu-
ally acquired. The restricted range of angles is due to issues related
to instrument calibration and problems in some scan angle ranges
(Narvekar et al., 2007; Gaiser et al., 1994). There are two types of
analysis carried out in this paper, azimuthal for testing spatial and
time series for testing seasonal, geophysical response. The T_v and T_h
primarily depends on incidence angle, whereas U and V have an addi-
tional strong dependency on azimuthal look angle. In order to satisfy
the WindSat primary mission goal of estimating the wind vector, pre-
cise measurements of all Stokes parameters are required. The order
of magnitude of the U and V parameters is a few Kelvin and, there-
fore, a small instrument bias can result in significant contamination
of these measurements. This may result in a shift in the level of the
retrieved parameters. Effects are expected to be more significant near
the swath edges. The dense forest cover in Brazil is an azimuthally
isotropic area and has been used as a hot calibration target in studies
of data quality of spaceborne radiometers, such as AMSR-E (Njoku

et al., 2004). In order to reduce bias contamination of the geophysical signatures in the U and V parameters, the entire data is analyzed over Brazil rain forest location (Narvekar et al., 2007). Figure 3.4 shows the scatter plot of the 10.7 and 37 GHz U with instrument scan angle for September 2003. The different colored points indicate the mode of data acquisition. The instrument bias associated with higher positive is apparent.
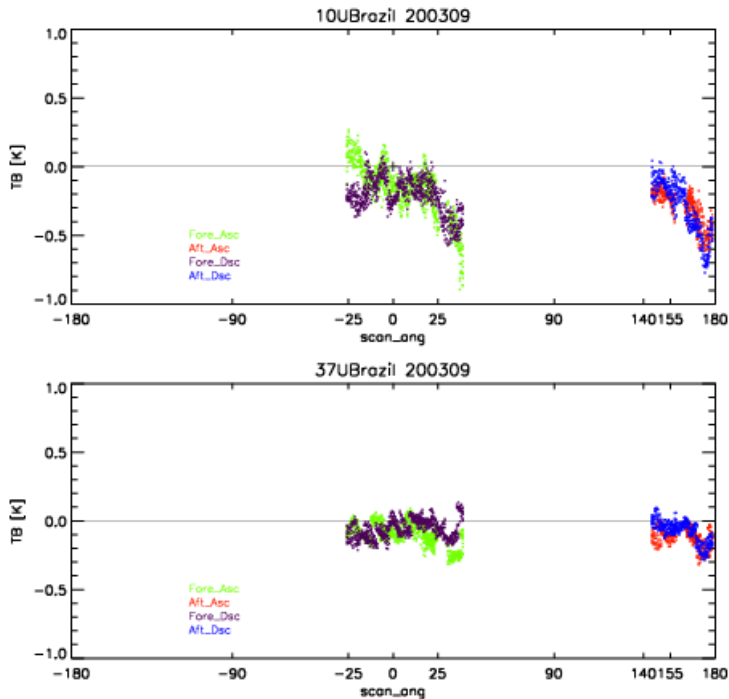

Figure 3.4: The 10.7 and 37 GHz U parameter plotted with instrument scan angle, different color points indicates different mode of data acquisition.

These effects are expected to be more significant near the swath edges. In order to reduce bias contamination of the geophysical signatures of the U and V parameters, we have restricted our entire analysis to scan angles between -25° +25° in the forward swath. Bias associated with this scan angle range is expected to be smaller than
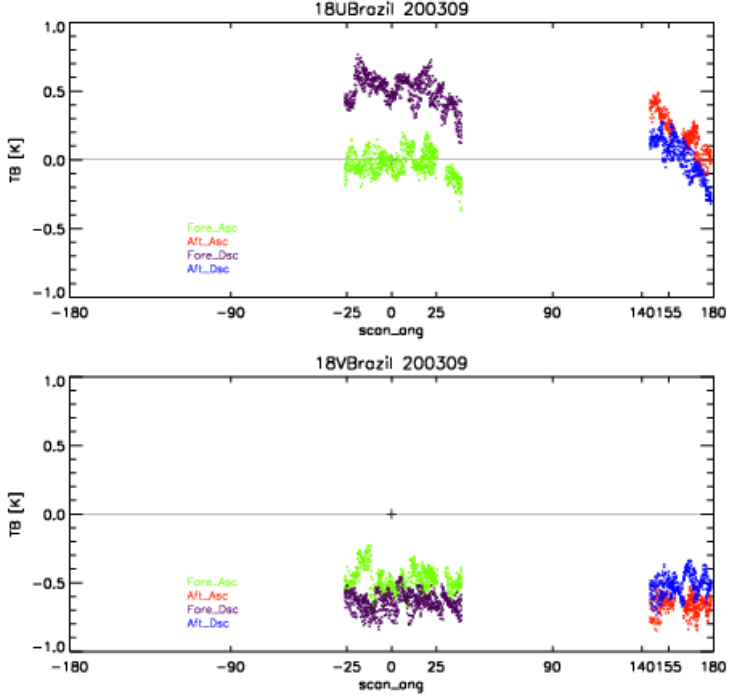
Figure 3.5: The 18.7 GHz U and V parameters plotted with instrument scan angle, different color points indicates different mode of data acquisition.

the rest of the scan angle range. Similar was observed for all other months. In a previous WindSat land surface study (Narvekar et al., 2007), the scan angle was restricted to -25° to +25° that is least affected. However, this range of instrument scan angle results in a small coverage of the azimuth angle,φ_{rad}, which highly reduces the reliability of any understanding drawn from azimuthal analysis. Therefore, we also consider a small scan angle range (15°) from 140° to 155° of the aft swath, which shows good agreement with the +25° to -25° scan angle of the forward swath.

The selected scan angle range is also applicable at 37 GHz frequency. Published results for WindSat have shown that the 18.7 GHz measurements are the most effected by the calibration bias (Twarog

et al., 2006). Figure 3.5 shows the plots of 18.7 GHz U and V for the same period as of Figure 3.4. The U component shows a shift of 0.5 K for the fore descending, which is slightly lower for the maximum of aft ascending. On the other hand, the V component shows the average shift of around -0.5 K in all the channels. The problem in the 18 GHz channel was also observed for the other spaceborne radiometers, such as Multichannel Scanning Microwave Radiometer (MSMR), operating at similar frequencies, as of WindSat (Rao et al., 2006). Some of the published results of AMSR-E hence also shown higher variability at 18 GHz channel. The 18 GHz band lies close to the water vapor band. Presently, the reason for this effect observed in WindSat 18.7 GHz is not investigated. Hence, for the current study we have excluded the 18.7 GHz observations.

For carrying out temporal analysis the data is usually averaged over the study area on given date. To avoid any significant azimuthal modulation in the daily average, the selected scan angle range of $+10°$ to $-10°$ in forward swath is used, unless specified. The following section presents the description of the study areas.

4 Polarimetric Observations over Land

WindSat provides an opportunity to explore the passive microwave polarimetric signatures of land surfaces. Large homogeneous regions with unique features were identified. These included forest, rangeland, desert and agricultural conditions. WindSat observations at horizontal and vertical polarizations over land surfaces were found to be well calibrated and consistent with other passive microwave sensors. Isotropic regions (e.g. Amazon Rainforest) had no polarimetric response at all azimuth angles. Results showed that land surfaces with aligned features (topography or row structured vegetation) produced systematic variations in the 3rd and 4th Stokes parameters. These responses were found to be in good agreement with pervious studies of the sea surface as well as a spaceborne scatterometer study. Analysis of temporal trends of the variation in polarimetric measurements for a specific azimuth angle could be attributed to crop growth cycle in the agricultural region. Further analyses will seek to isolate specific features that could be used in applications such as soil moisture retrieval.

4.1 Background

Passive microwave remote sensing has been shown to be a valuable source of information for land applications such as large scale soil moisture retrieval. A limitation of these retrievals is that there are often more parameters that need to be determined than there are independent observations. These parameters include multiple scales of roughness and potentially several vegetation characteristics. One way to deal with this issue is with ancillary data sources. However,

this can be challenging and a retrieval based upon a single sensor may be more easier.

Traditional spaceborne microwave radiometers have provided multi-frequency dual polarization data. New information and opportunities for improved retrievals might be possible with fully polarimetric instruments. The WindSat instrument provides the first spaceborne fully polarimetric microwave measurements of the Earth's emission. The primary objective of the WindSat is to provide information for sea surface wind vector (speed and direction) retrievals. The data is also acquired over land surfaces and thus offers new opportunities to investigate the possibility of introducing fully polarimetric measurements in land surface applications. As a first step in the analyses, data over several large and homogeneous regions were extracted over an extended period. The response of WindSat at different frequencies for vertical and horizontal polarizations was observed over wellknown calibration targets. An attempt was also made to investigate the possible land surface structural information present in the U and V parameters. It is possible that the information present in these parameters may be helpful in improving the retrieval of land surface geophysical parameters.

4.2 Polarimetric variables and expected responses

Passive microwave polarimetry has been extensively studied for sea surface applications, but very little has been investigated over land. The launch of WindSat has provided an opportunity to study the polarimetric measurements of the Earth's emission from space. In this section a basis for WindSat polarimetry of land surfaces is developed from theoretical models (Tsang, 1991), previously conducted airborne passive polarimetric studies over ocean surfaces (Yueh et al., 1994; Yueh, 1997), and ground based studies over land surfaces (Sobjaerg and Skou, 2003; Pham et al., 2005; Nghiem et al., 1991).

For sea surfaces the response of the U and V parameters is primar-

ily dependent on sea surface roughness, which is a function of wind vector (Yueh, 1997). A two-scale sea surface roughness approach has been found to yield better results in the wind vector retrievals. The 'two-scale' refers to two levels of roughness, one from large waves on the order of meters and the other from small capillary waves on the order of centimeters, which lay on top of large scale waves (Yueh, 1997). These studies also showed the dependency of U and V on the azimuth look angle of a radiometer. In that study, all Stokes parameters were represented as second harmonic sine functions of the relative azimuth angle, $\varphi_{relative}$, as presented in Equations (2.34 to 2.37). In these relations, the first harmonic primarily accounts for up-wind and down-wind asymmetry and the second harmonic accounts for up-wind and cross-wind asymmetry (Yueh, 1997). The up-wind, down-wind and cross-wind in terms of only the gravity waves can be expressed in terms of slopes of these waves in the leeward, windward and in the direction perpendicular to leeward or windward, respectively. Usually, the polarimetric signal produced by gravity waves gets modified by small scale capillary waves superimposed on these waves. The harmonic dependency of U and V on the orientation of the sea waves results in negative or positive values of these parameters.

In translating the results described above to the land surface, the orientation of topographic slopes of different scales ranging from kilometers to centimeters is expected to produce responses in the U and V parameters. In the present study we have symbolized the orientation of the land surface structure by φ_{orient}, which is equivalent to φ_{wind} in terms of sea surface.

For land surfaces, Tsang et al.(1985) derived theoretical expressions for all Stokes parameters. In that study, the non-zero 3rd and 4th Stokes parameters were considered a result of land surface roughness and were also expressed as a function of azimuth angle. Ngheim et al.(1991) conducted a ground based experiment and showed the azimuthal dependency of brightness temperature on soil surface structure. In that study, a periodic soil surface was created and measurements were made for the horizontal (h), verticle (v) and 45° polarization planes at different azimuth angles. The 45° T_{B} along with the difference between h and v was used to calculate the U parameter.

In the presence of vegetation, the Stokes parameters are expected to depend primarily on biomass structure. The few available ground based experimental studies that have been conducted have shown the dependency of polarimetric measurements on agricultural field rows and crop structure (Sobjaerg and Skou, 2003; Pham et al., 2005). In these studies, measurements over an agricultural field were acquired during different stages of crop growth. In the absence of vegetation, a plowed soil surface produces a polarimetric signal, which decreases as rainfall smooths the surface. When there was vegetation, the biomass structure produced a polarimetric signal that is likely to be a function of crop height and field row orientation. These studies also showed that the V signal is $180°$ out of phase with U, which also agrees with the sea surface studies. The scale of V variation was found to be 1/4th of U, which was also observed for sea surfaces (Yueh, 1997; Sobjaerg and Skou, 2003). The physical definition (Gaiser et at., 2004) of the V component indicates its dependency on the phase difference between the vertical and horizontal T_{B} measurements. In case of a sea surface, the wavelengths of the capillary waves are on the scale of centimeters and may have an impact on V measurements at WindSat frequencies. However, for the land surfaces it is much more complex to define such a centimeter level structure that is expected to result in non-zero V, especially over a footprint size of WindSat.

In general, land surfaces can be considered as highly variable with different levels of roughness coming from different surface features of the Earth, such as terrain on the scale of kilometers, smaller topographic variation on the scale of meters, roughness at a centimeter scales. In the presence of a vegetation cover, the primary effect of vegetation structure is expected in the polarimetric signature. The vegetation structure may be considered as a plant or tree structure along with the height or orientation of agricultural field rows.

4.3 Study Areas

Further understanding of the passive microwave polarimetric features of land surfaces would benefit from observations of well known sites.

At present, one source of data is the WindSat sensor. Developing an observation based analysis using coarse spatial resolution satellite data is challenging for the following reasons;

• All of the surface and vegetation effects described above can occur individually or at the same time.

• They can also vary with time (plant growth cycle or soil moisture from precipitation)

• The azimuth angle changes with each pass.

• The exact footprint center will rarely ever be the same (pass to pass).

• Spatial variations will typically occur at scales much smaller than a WindSat footprint, which means there could be a mixture of conditions.

Our approach to limiting the impact of these issues was to use study sites that;

• Had uniform conditions over a spatial domain larger than a satellite footprint.

• Represents diverse conditions.

• Use areas large enough so that frequent temporal observation were possible for a fixed range of azimuth angles.

As a result four sites across the glob are selected (Figure 4.1) as described below;

1.Amazon rainforest in Brazil (Lat: -7.5° to -6.5° Lon: -66.0° to -65.0°): This area represents a dense vegetation condition that remains invariant throughout the year due to abundant rain fall (around 2500 mm, annually). It has been used previously (Njoku et al., 2004) as a vicarious calibration hot target because of the consistent long term behavior of T_v and T_h. Secondly, the presence of dense vegetation makes the emission generated in all polarization planes similar, making this area highly isotropic in nature. The isotropic area determines the reliability of U and V measurements, since for these areas U and V are expected to be 0 K.

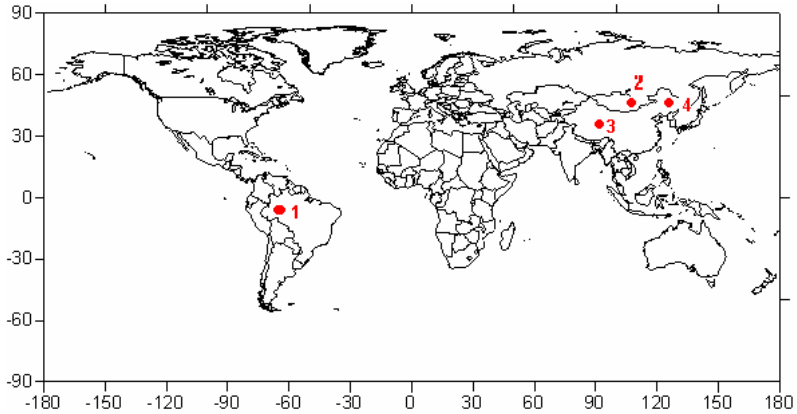2.Rangelands in Mongolia (Lat: 45.8° to 46.8°, Lon: 106.1° to 107.5°):

Figure 4.1: The study area locations.

This area represents lightly vegetated grassland conditions. Occasional rain events are expected in summer months, and snow may occur in winter (November to January). The study area is well instrumented for in situ soil moisture measurements and has been used for validating satellite soil moisture retrievals (Jackson et al., 2004). Low topographic variability under sparse vegetation provides a homogenous isotropic target for testing U and V responses under varying soil moisture conditions.

3.Taklamakan Desert in China (Lat: $37.5°$ to $38.5°$, Lon: $82.5°$ to $83.5°$): is a cold desert with a highly structured sand surface in the North West part of China. The presence of large sand dunes makes this area a highly anisotropic target. These large structures, easily seen in Figure 4.12, are oriented north-east with their slopes facing north-west and south-east. Due to this systematic orientation over an area larger than the footprint of a radiometer, this area facilitates the study of WindSat U and V over the land. This site had been identified as an anisotropic target in (Bartalis et al., 2005).

4.Heilongjiang Agricultural area in China (Lat: $47.0°$ to $48.0°$, Lon:

125.0° to 126.0°): represents agricultural fields with almost all the field rows oriented north-south (Figure 4.16). The main crops grown are corn and soybean. The vegetation is present during summer months. In winter the region is mainly bare soils with possibility of snow. Features of this site had been studies in (Bartalis et al., 2005; Bartalis et al., in press).

4.4 Data analysis

In order to understand the temporal behavior of the Stokes parameters, time series plots for each study area were developed. In an analysis of land it is normally assumed that the azimuth angle has no significant effect on T_{B}. As a result, all footprints falling in the study area are usually averaged. For U and V we expect that there will be an azimuth angle effect on T_{B}. Therefore we limited our analysis to a specific range of scan angles ($\pm 10°$) for each site. This was a tradeoff between having adequate data over an area for temporal analysis and the effect of allowing the scan angle to vary even this much. It should be noted that there might be some residual variability associated with day-to-day variations in the mean scan angle over the area.

Another critical point of the azimuth angle is related to ascending and descending passes. The selected scan angle range for ascending and descending orbits corresponds to completely different azimuth angles with respect to north. In terms of the selected study areas, the scan angle between -10° to +10° corresponds to the azimuth angles range around 190° for descending passes and around 350° for ascending passes. To verify the land surface structural signature dependency on azimuth angle we have combined the time series of U and V observations of ascending and descending orbits in the next section.

4.4.1 Analysis over the Amazon rainforest

The brightness temperature is a function of the emissivity and surface temperature of the target under investigation (Ulaby, 1986). In the presence of vegetation the emission from the soil surface is attenuated.

In addition, vegetation adds its own radiation, which is unpolarized in nature (Jackson et al., 2005).

Figure 4.2: Arial photograph of the selected area in Amazon Rainforest in Brazil, The zoomed part shows the 1x0.8 Km area

For dense vegetation conditions such as the Amazon at WindSat frequencies, any emission from the ground surface would be masked by the canopy due to typically high levels of vegetation. Figure 4.2 shows the arial photograph of 10 km of the region selected and zoomed out 1 km area. Figure 4.3 shows the time series of averaged T_v and T_h over 50 x 50 km plotted for selected frequencies over an extended period.
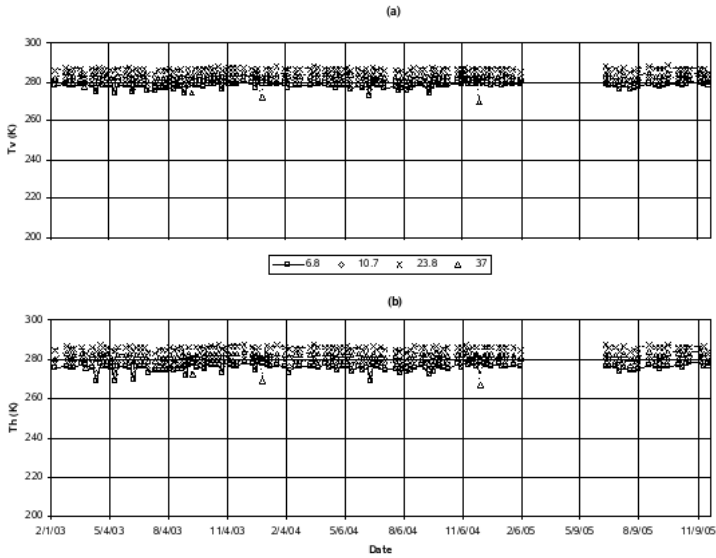
Figure 4.3: WindSat brightness temperature time series for 6.8, 10.7, 18.7 and 37 GHz for (a) T_v and (b) T_h descending observations, plotted for the period February 2003 to November 2005 for Amazon study area in Brazil.
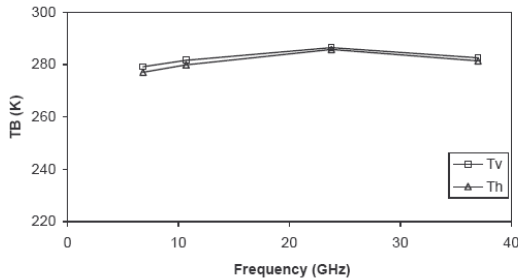

Figure 4.4: Brightness temperatures at vertical and horizontal polarizations plotted as a function of frequency for the study area of Amazon in Brazil. 188 data points averaged for October 2003. The standard deviation at each frequency was lower than 1.5 K.
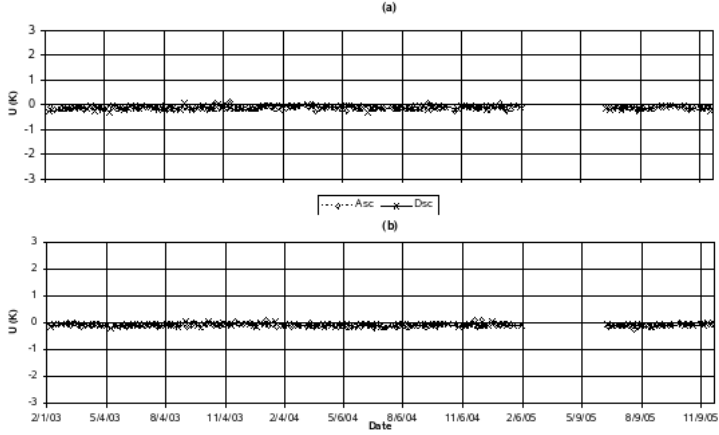
Figure 4.5: The 3rd Stokes parameters time series at (a) 10.7 GHz and (b) 37 GHz for the period of February 2003 to November 2005, for the Amazon Brazil. The ascending (averages around $190°$) and descending (averages around $350°$) observations at each frequency are plotted together to facilitate comparison.

There are a few low outlier points that are likely to be associated with very large rainfall and flooding. The range of observed brightness temperatures was found to agree with previous investigations (Calvet, 1994). Figure 4.4 shows the spectral plot of brightness temperatures for the study area. The nearly unpolarized nature of this particular dense vegetation results in values of T_v and T_h that are very similar at all frequencies, as expected (Jackson et al., 2005). The T_B at 37 GHz shows a small drop, which is likely due to the sensitivity of this channel to atmospheric extinction and surface scattering (Njoku et al., 2004). The surface scattering is caused due to the structure on top of the vegetation cover, which is sensitive to 37 GHz due to its low penetration inside the canopy. The long term invariant nature of the Amazon is apparent in Figure 4.3. The brightness temperature fluctuates within the same range over an extended period. This
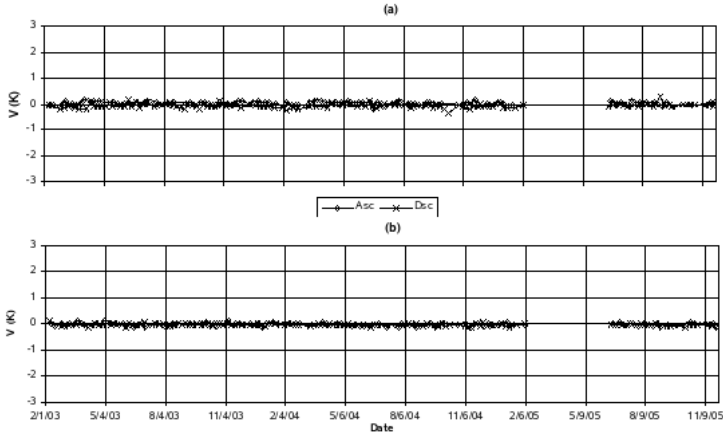
Figure 4.6: The 4th Stokes parameters time series at (a) 10.7 GHz and (b) 37 GHz for the period of February 2003 to November 2005, for the Amazon Brazil. The ascending (averages around 190°) and descending (averages around 350°) observations at each frequency are plotted together to facilitate comparison.

characteristic of the region makes the Amazon useful as a suitable calibration (thermal stability) target for the instrument.

The times series of 10.7 and 37 GHz U and V for the Amazon study area are plotted in Figures 4.5 and 4.6, respectively. The U and V parameters for an isotropic area are expected to be zero. The WindSat 10.7 GHz U and V measurements support this assumption that the area is isotropic. A small shift ($\approx$0.1 K) from zero was observed that is likely the result of an instrument bias.

Secondly, the absolute error when measuring U and V is set to 0.25 K (Gaiser et al., 2004) and hence, any fluctuation below this range can be considered to be due to instrument noise. The T_{B} scale in Figures 4.5 and 4.6 was chosen to facilitate comparison with other selected anisotropic areas (e.g. Taklamakan in China), where the signal strength will reach up to 3 K. The long-term invariant U and V parameter at both frequencies reflects the invariant nature of the

Amazon; this also supports the reliability of the WindSat U and V
channels. Similar trends were found for the 37 GHz channel.

4.4.2 Mongolia rangeland

The selected area located in Mongolia is instrumented for in situ
soil moisture measurements. Jackson et al.(2004) have investigated
this area for soil moisture retrieval using Advanced Microwave Scan-
ning Radiometer (AMSR-E) observations. We expect the region to be
isotropic but since it is lightly vegetated we can examine the response
of U and V to temperature and soil moisture variations. Figure 4.7
shows the aerial photograph of the area and a photo taken at one of
the in situ measuring station.

46° 24'N 107° 38'E

Figure 4.7: Study area location in Mongolia

Figure 4.8 shows the time series of T_v and T_h for selected WindSat
frequencies. An annual temperature trend is apparent in this figure,
with brightness temperature varying over the range of ≈ 60 K for both
polarizations. Several low spikes in the observations of T_h, mostly for
6.8 and 10.7 GHz, are the result of increases in soil moisture due to
rain events. It is generally accepted that T_v at 37 GHz is mainly a
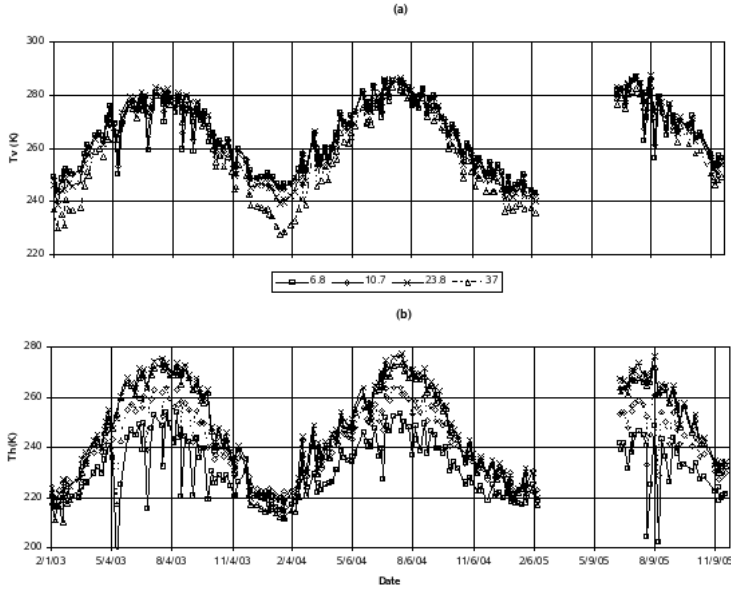function of surface temperature (De Jeu R.A.M., 2003). The spectral

Figure 4.8: WindSat measured brightness temperature time series for 6.8, 10.7, 18.7 and 37 GHz for (a) T_v and (b) T_h descending observations, plotted for the period February 2003 to November 2005 for Rangelands of Mongolia.

difference between 37 GHz T_v and a lower frequency is important in snow related studies (Fung, 1994).

In Figure 4.8 the T_v at 37 GHz shows a significant drop in brightness temperature, as compared to the other frequencies, during the winter months (November to February) of 2003. The gound based stations at mongolia and their data available at Hydrology and Remote Sensing Lab., United States Dept. of Agriculture (USDA) indicates snow cover over this area during winter 2003. The higher signal of U may be the result of the presence of snow during that period. However, this drop was not apparent during the 2004 winter.

Figure 4.9 shows the spectral plot of T_v and T_h over the Mongolia rangeland study area. A time period must be selected in order to have an adequate sample size ($\approx$200). However, averaging highly variable
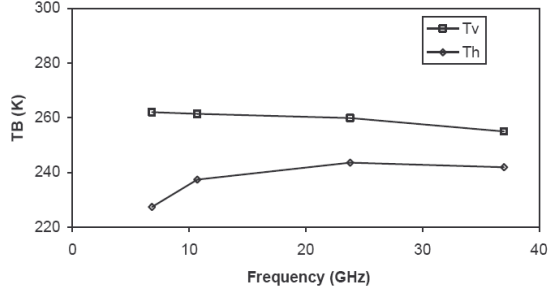
Figure 4.9: Brightness temperatures at vertical and horizontal polarizations plotted as a function of frequency for the study area of Mongolia. 282 data points were averaged for October 2003. The standard deviation for each frequency was smaller than 2 K.
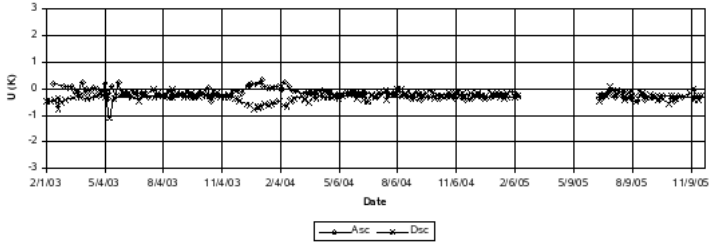

Figure 4.10: The 3rd Stokes parameters time series at 10.7 GHz for the period of February 2003 to November 2005, for the Rangelands of Mongolia. The ascending (averages around $190°$) and descending (averages around $350°$) observations at each frequency are plotted together to facilitate comparison.

Figure 4.11: The 4th Stokes parameters time series at 10.7 GHz for the period of February 2003 to November 2005, for the Rangelands of Mongolia. The ascending (averages around 190°) and descending (averages around 350°) observations at each frequency are plotted together to facilitate comparison.
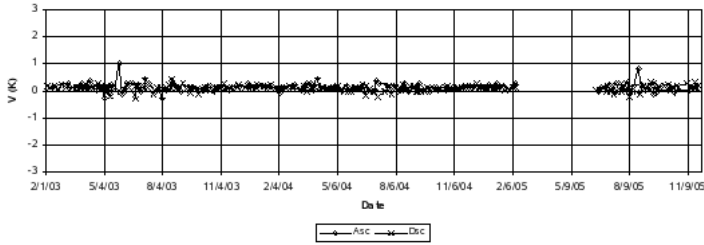
conditions is not useful. Therefore, we chose the month of October 2003 when no spikes are present in an attempt to minimize temperature variations over time. From theory (Ulaby et al., 1982), the dielectric constant should decrease with increasing frequency, which should result in an increasing emissivity and increasing brightness temperature.

The T_v is mainly a function of temperature and T_h to be mainly a function of the dielectric constant (De Jeu R.A.M., 2003). As a result, T_h is expected to have larger variations between the brightness temperatures at different frequencies as compared to T_v. In addition, parameters such as penetration depth, atmospheric conditions and surface scattering also affect this relationship. The trends in Figure 4.9 are typical of bare or lightly vegetated soils (Jackson et at., 2005). The larger changes from 10 GHz to 6 GHz T_h are likely to be associated with surface roughness and vegetation effects as well as a difference in the effective temperature contributing to the measurement.

As noted previously, the Mongolia area facilitates the examination of U and V responses for soils with low amounts of vegetation, small

topographic variations, and some significant soil moisture variability. Figure 4.10 and 4.11 shows the 10.7 GHz U and V plots over the investigation period. Ascending and descending U observations show good agreement except for the winter months of 2003. The 37 GHz measurements also show similar trends (not shown here), but exhibited additional variability during the 2004 winter. Based upon the T_v and T_h analysis, it was concluded that during the winter period of 2003 there might be snow cover that results in the U response and a difference between ascending and descending observations. If the winter months are excluded from the analysis, then the U and V results indicate that the region is isotropic and that soil moisture variations (obvious in the T_v and T_h data) do not affect U and V measurements.
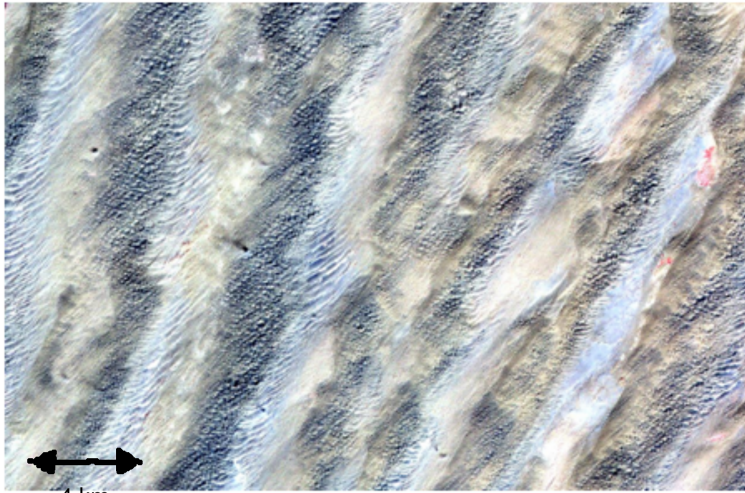
4.4.3 Taklamakan Desert

The Taklamakan desert in western China was chosen for the study of WindSat polarimetric (U and V) signals over structured bare soils. Bartalis et al.(2005) used scatterometer observations over the Takalamakan desert to demonstrate the importance of the scan angle over structured regions.

The area consists of large sand dunes oriented north-east with their slopes facing the south-east and north-west, see Figure 4.12. Sand dune orientation in a specific direction over the entire region (larger than a WindSat footprint) provides an opportunity to investigate the impact of land surface structure on the polarimetric signals. Initially, the T_v and T_h response is analyzed (Figure 4.13). The annually temperature trend is apparent in the Figure 4.13. The response of T_v and T_h is similar to that of Mongolia area discussed earlier and is as expected for bare soils. The 10.7 and 37 GHz U and V time series are shown in Figure 4.14 and 4.15. The U observations for ascending orbits (positive T_B) are inversely related to the descending orbits (negative T_B) for both frequencies (Figure 4.14). Unlike for Amazon rainforest, the response for the U channels are clear anisotropic.

The scan angle range corresponds to radiometer azimuth angles with respect to north (φ_{rad}) for descending ($\approx 190°$) and ascending

(a)

4 km

(b)

Figure 4.12: Advanced spaceborne thermal emission and reflection (a) Arial photograph and (b) radiometer (ASTER) images over Taklamakan, desert area in China, acquired on 25th August 2005.
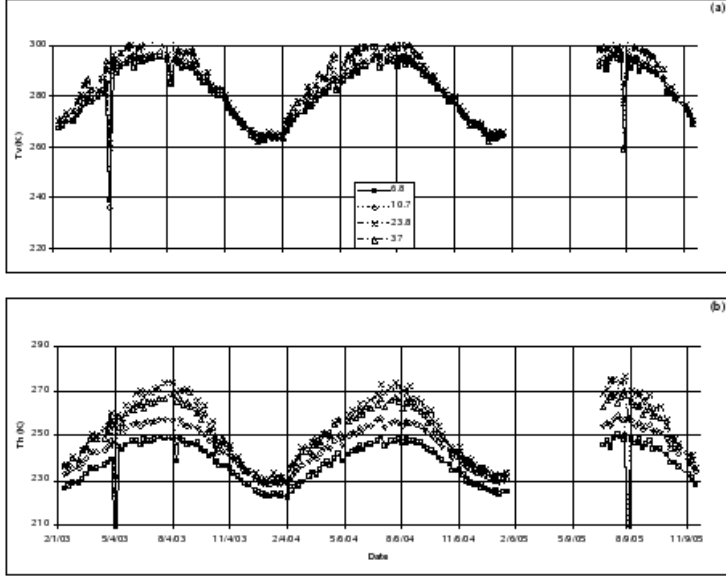
Figure 4.13: Time series of T_v and T_h for the period June 2003 to November 2005.

passes ($\approx 350°$). The large topographic structure of the Taklamakan desert surface is analogous to large ocean waves, with the slopes of the sand dunes oriented south-east ($\approx 120°$ w.r.t. north) and north-west ($\approx 300°$ w.r.t. north). The south-east slopes are oriented along the upwind direction (in the direction of prevailing winds), giving a land surface orientation angle of $\approx 120°$. The relative azimuth angle, $\varphi_{relative}$, is the difference between the orientation of the land surface features and radiometer azimuth angle. The was estimated to be $\approx 290° \pm 8°$ for descending orbits and $\approx 130° \pm 8°$ for ascending orbits. From theory and aircraft observations (Yueh, 1997; Fung, 1994), for a relative azimuth angle of $290°$ the U response is expected to be positive and for $130°$ the response is expected to be negative. However, these observations have the opposite signs for both the ascending and descending angles. This is due to the definition of the U and V for
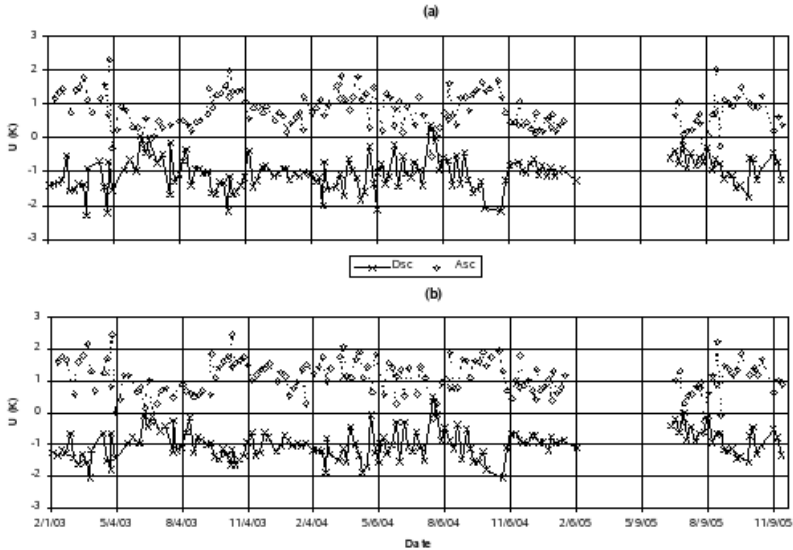
Figure 4.14: The 3rd Stokes parameters time series at (a) 10.7 GHz and (b) 37 GHz for the period of February 2003 to November 2005, for the Taklamakan desert study area in China. The ascending (averages around $190°$) and descending (averages around $350°$) observations at each frequency are plotted together to facilitate comparison.

WindSat, which have opposite sign as seen from the aircraft data (Yeuh et al., 1994) (Figure 4.15). These results clearly demonstrate the presence of a structural signature in the WindSat U parameter over a structured bare soil surface. Although we observed a response for the U parameter, no significant variation was observed in the V response in either temporal or azimuthal analyses (Figure 4.15). The ascending and descending observations were found to be close to zero.

4.4.4 Heilongjiang Agriculture

The Heilongjiang agriculture area in north China was chosen to study the WindSat polarimetric response for structured vegetation. This area consists of numerous small agricultural fields with almost all the field rows oriented very close to North-South direction. Figure 4.16
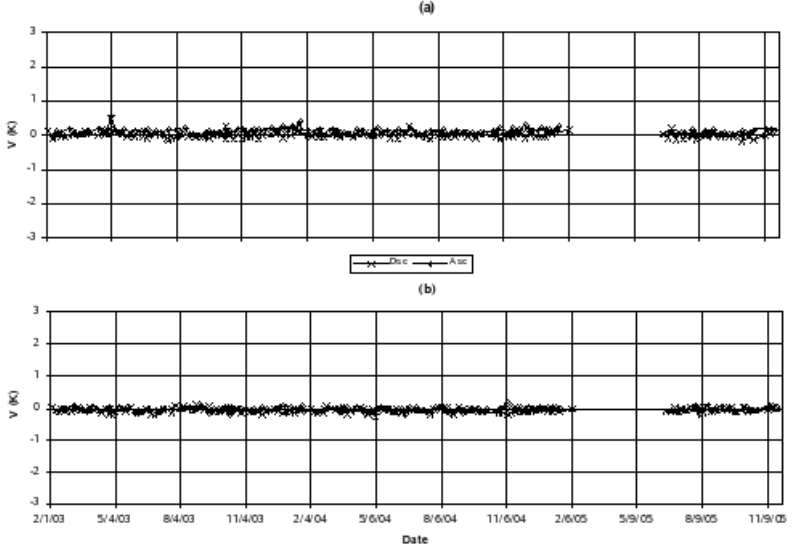
Figure 4.15: The 4th Stokes parameters time series at (a) 10.7 GHz and (b) 37 GHz for the period of June 2003 to January 2005, for the Taklamakan desert study area in China. The ascending (averages around 190°) and descending (averages around the 350°) observations at each frequency are plotted together to facilitate the comparison.

clearly shows the regional pattern. From this image the field structure orientation angle is estimated as = 80°.

A previous ground-based study conducted at L-band (Sobjaerg and Skou, 2003) showed a dependency of the U and V parameters on vegetation rows and height. This particular site had been identified in (Bartalis et al 2005; Bartalis et al, in press) as a target with a possible polarimetric response using backscatter coefficient data that showed a clear second harmonic dominance in the azimuth dependance. Figure 4.17 shows the T_v and T_h times series. The spikes in the T_B value causing lower brightness temperature is due to an increase in the soil moisture due to rain events. The 6.8 GHz is more sensitive to the dielectric constant and hence the soil moisture and, therefore, the response is higher at this frequency (Jackson et al., 2005). The 10.7 and 37 GHz U time series are plotted in Figure 4.18. The ascending
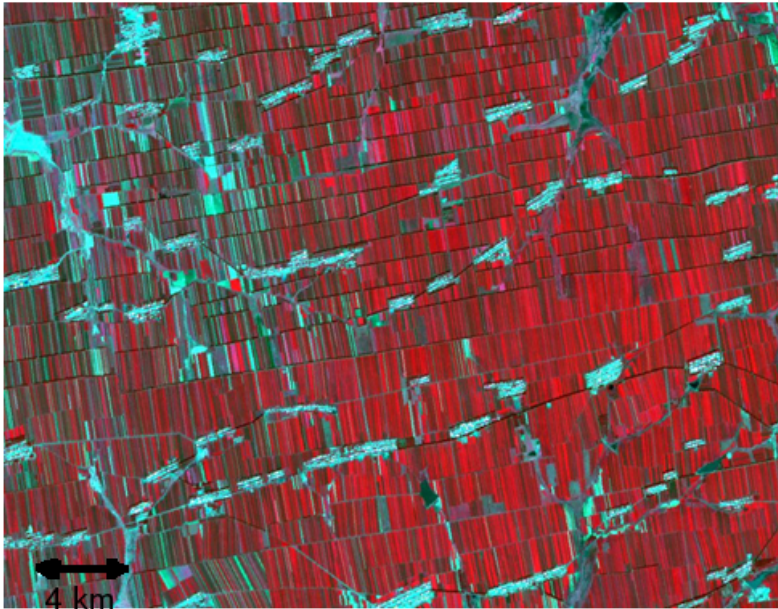
Figure 4.16: The ASTER image of Helonjiang agricultural area of China acquired on 25th August 2005.

observations lie close to 0 K whereas the descending data have negative values during the summer months, with the maxima occurring during July of both years. During winter, this area is predominantly bare soil and observations during these months exhibit no response for U and V. The summer period response was larger for 10.7 GHz as compared to 37 GHz. The lower frequency of 10.7 GHz increases the potential canopy penetration and as a result, different components of the vegetation may contribute to the signal at different frequencies.

Because for ascending orbits is $\approx 350°$ and $\approx 190°$ for descending, for the Heilongjiang area the relative azimuth angle is $\approx 90°$ for ascending and $\approx 250°$ for descending passes. Based upon results presented in (Yueh, 1997; Yueh et al., 2006), a relative azimuth angle of 90Åř should result $U = 0$ K, and 250° should result in a positive value. Again, note that the definition of the U and V of WindSat is off by a
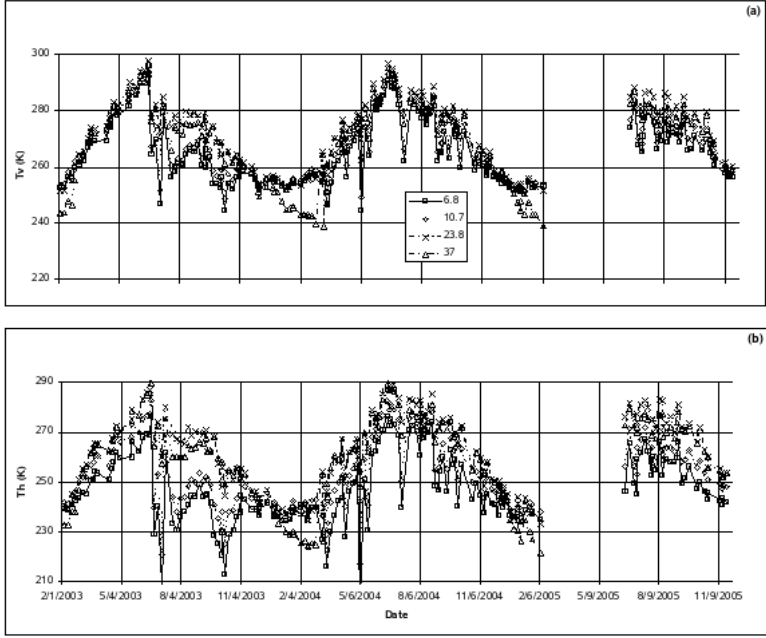
Figure 4.17: The T_v and T_h times series plotted for the frequencies 6.8, 10.7, 23.8 and 37 GHz.

minus sign from the aircraft data (Yueh et al., 1994a). The ascending and descending U observations agree with the theory, with ascending observations showing T_B fluctuating around a small negative value that we interpreted as sensor bias. The descending data had negative values. Further examination of this data was conducted by separating the available azimuth angle range of $+25°$ to $-25°$ for ascending passes into $10°$ increments. Figure 4.19 shows the time series for three scan angle intervals; $-25°$ to $-15°$, $-5°$ to $+5°$ and $+15°$ to $+25°$ (ascending orbits).

These three scan angle intervals correspond to radiometer azimuth angles of $\approx 10°$, $\approx 350°$ and $\approx 330°$, respectively. From the satellite image shown in Figure 4.16, the orientation of the field rows is approximately $\approx 350°$, which is almost the same as the direction of the
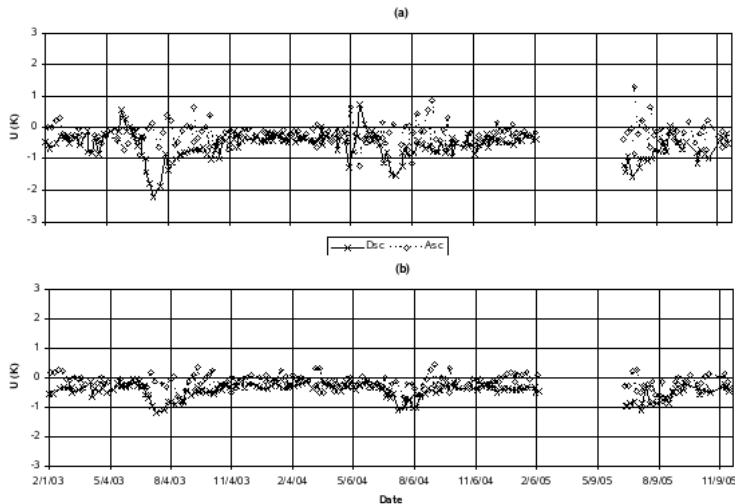
Figure 4.18: The 3rd Stokes parameters time series at (a) 10.7 GHz and (b) 37 GHz for the period of February 2003 to November 2005, for the Heilongjiang agricultural study area eastern China. The ascending (averages around 190°) and descending (averages around 350°) observations at each frequency are plotted together to facilitate comparison.

ascending pass. From theory, for an azimuth angle of 350°, the -45° and +45° polarized T_{B} should be similar.

Any deviation from this scan angle range is expected to produce different brightness signals in the 45° channels, resulting in a non-zero U value. Figure 4.19, shows this effect very clearly. The U observations for the 350° azimuth angle range fall between the observations of the 10° and the 330° azimuth angle ranges. The relative azimuth angles for 10° and 330° are estimated to be ≈ 20° and ≈ 340°, respectively. As per the theory, U at a relative azimuth angle of 20° should be positive and at 340° it should be negative. The curves of Figure 4.19 agree with the theory and, therefore, demonstrate that structured vegetated conditions can produce a U signature.

The time series of the 10.7 and 37 GHz V channels for the Heilongjiang agriculture region are shown in Figure 4.20. Recall that no V response was observed for the structured bare soil of the Takla-
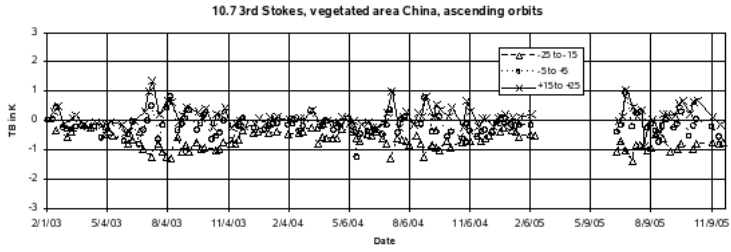
Figure 4.19: WindSat 10.7 GHz 3rd Stokes parameter three time series plotted for the scan angle intervals between -25° to -15°, -5° to +5° and +15° to +25° of ascending orbits, for the Heilongjiang agriculture region in China.
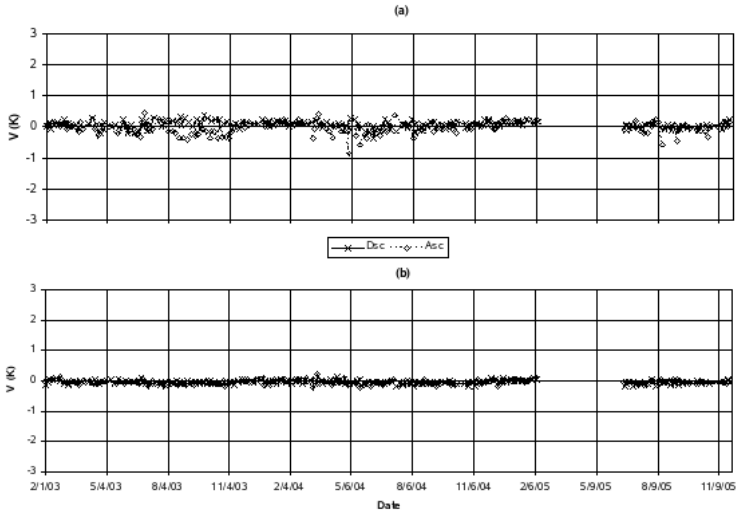
Figure 4.20: The V component time series at (a) 10.7 GHz and (b) 37 GHz for the period of February 2003 to November 2005, for the Heilongjiang agricultural study area in eastern China. The ascending (averages around 190°) and descending (averages around 350°) observations at each frequency are plotted together to facilitate comparison.

makan desert. However, for this agricultural region a systematic V response was observed in the 10.7 GHz observations between August and October. The V signal appears to lag the U observations. This is likely to be related to either senescence of the vegetation or harvesting. The ascending observations were negative and the descending were positive. From Yueh 1997, the V responses should be 180° out of phase compared to U parameter. The WindSat V measurements show good agreement with the theory for the U parameter (Figure 4.18). The 37 GHz V data did not have the same response as 10.7 GHz. Both the ascending and descending observations are close to zero (Figure 4.20). This result suggests a possible canopy penetration effect, 37 GHz is not expected to sense as deep into a canopy as 10 GHz. These preliminary results also clearly warrant a more rigorous analysis of the V parameter for vegetation.

4.5 Conclusions

Polarimetric passive microwave measurements may provide new information that can be used to estimate or describe land surface features. Data from the WindSat instrument were used in this study to determine if this was possible. Issues of satellite footprint size placed demands on experimental design. As a result, four large and homogenous regions were identified that represented unique land surface features.

The analysis of the Amazon rainforest data showed consistency for T_v and T_h over a densely vegetated area. The U and V observations demonstrated the invariant isotropic nature of the region and the reliability of the sensor data. The Mongolia rangeland site was selected to represent isotropic conditions with less vegetation and time varying temperature and soil moisture. The U and V responses over this area were very close to zero for most of the year. From this we concluded that there was no soil moisture effect present in the U or V measurements. The Taklamakan desert area in China is topographically anisotropic and this gives rise to significant responses of the U parameter to the observed dune structure. The time series of the U parameter also agreed with sea surface polarimetric theory. The U and V

parameters for the Heilongjiang agriculture region showed structural dependency in the presence of agricultural crops. The trend of the U parameter was found to agree with ground based studies made with a L-band polarimetric radiometer.

The results of this study clearly show that when aligned land surface features are present, then there will be a response in the U channel. This is the first time this has been observed at satellite footprint scales. Further studies under controlled conditions of vegetation features are needed to refine our understanding. How to use this new information in application such as soil moisture retrieval is the next challenge.

5 Polarimetric Emission Over Antarctic Ice Sheet

In addition to its primary mission, WindSat also provides us with an opportunity to investigate the geophysical information content of fully polarimetric observations of land targets. A region of great importance is the Antarctic ice sheet, the coldest region on Earth, which plays an important role in the global climate acting as a thermal heat sink for the atmosphere and also as an indicator for global warming. Due to its great expanse and remote location, remote sensing is a valuable tool in monitoring. Seasonal and long term variations of the geophysical properties of the ice sheet have been studied using spaceborne active and passive microwave sensors (Long and Drinkwater, 2000; Njoku et al., 2004). Active observations primarily depend on the geometric features, such as topography and roughness, whereas the passive observations primarily depend on the dielectric and thermal properties of the surface and the subsurface of the Antarctic ice sheet. Moreover, surface and volume scattering influence the radiation emitted by the snow and ice. Passive observations have shown to have potential in estimating surface and subsurface temperature of snow and ice firn (Tsang et al., 1985). Additionally, the applicability of active and passive observations in estimating other geophysical quantities such as snow density and grain size, is also demonstrated (Long and Drinkwater, 2000; Drinkwater and Bingham, 2000). Some studies have combined active and the passive observations in order to better understand the scattering, emission and thermal properties and their annual variability over some locations in Antarctica (Long and Drinkwater, 2000; Drinkwater and Bingham, 2000). However, combining data from different sensors may be challenging due to the different resolution, incidence and azimuth angles, shift in the footprints and

the time of overpass. The present study examines what contribution
the fully polarimetric passive observations of WindSat can make to
better estimating the scattering, thermal and emission properties of
Antarctic ice sheet using a single sensor. As seen from the perious
Chapter 4, a non-zero U component can be caused by surface topog-
raphy and differently scaled roughness (Tsang, 1991; Yueh et al., 1994;
Narvekar et al., 2007).

Initial WindSat analyses have shown U and V signals of much
higher magnitude over snow and ice (Narvekar et al., 2006; Liu and
Weng, 2005) compared to those observed over open water, bare soil
and vegetated surfaces. The sea surface wind vector estimates from
polarimetric radiometers are in good agreement with those obtained
from scatterometer observations (Yueh et al., 2006).

In this Chapter, scatterometer studies carried out over the Antarc-
tic ice sheet (Long and Drinkwater, 2000) are used to develop a basic
understanding of the U and V signal. Rotschky et al.(2006) related the
magnitude of the scatterometer backscatter coefficient to the orienta-
tion of snow surface features, such as topographic slope and sastrugi
(periodic snow structures caused by the katabatic winds). The mag-
nitude of the backscattering coefficient also varies with the snow mor-
phological properties, such as density, grain size, and wetness (Bing-
ham and Drinkwater, 2000; Rotschky et al., 2006).

Section 5.1 describes the study areas. Section 5.2 analyzes T_v and
T_h in the light of studies previously carried out at similar frequen-
cies. These results are used as a reference for the U and V studies.
Section 5.3 analyses the azimuthal anisotropy of U and V for snow
and ice. A second harmonic function is used for fitting the azimuthal
distribution of the U and V in Section 5.4. The results are compared
with scatterometer derived snow feature orientation maps. Section 5.5
discusses the seasonal variability of the U and V. The understanding
developed over selected study locations are extended over the entire
Antarctic ice sheet in Section 5.6. Section 5.7 gives the conclusions of
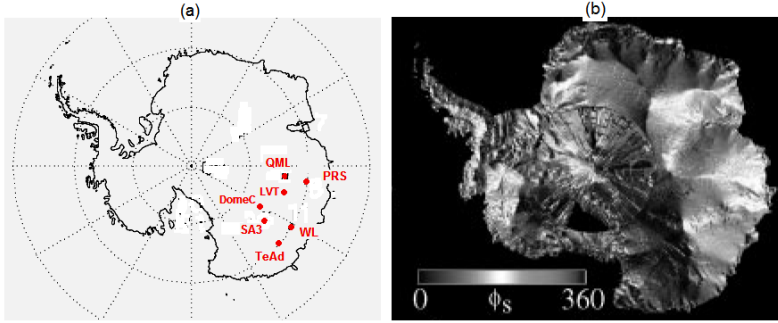the study.

Figure 5.1: Maps of Antarctica (a) showing locations of the selected study areas, i.e. Dome C, Queen Mary Land (QML), Study Area 3 (SA3), Lake Vostok (LV), near Pionerskaya Russian Station (PRS), Wilkes Land (WL) and Terre Adelie (TeAd) and (b) direction of local topographic slope w.r.t. north (adopted from (Long and Drinkwater, 2000)).

5.1 Study areas

In Antarctica the temperature remains below freezing most of the year. The climatic conditions mainly differ between the coastal (lower altitudes) regions with a short melting season and the interior (high altitudes) continent, where melting never occurs. The snow deposition rate is higher in the coastal area where it may reach above 1000 kg/m^2/a, while in the interior it may be as low as 1 kg/m^2/a (Massom et al., 2004). In the coastal areas, summer melting of the deposited snow occurs. The regions with higher altitudes receive little annual snow fall, on the order of few centimeters per year, and temperatures are below freezing most of the time. One of the high altitude research stations ($\sim$3000 m) is Dome C (74.5 S/ 123 E). The annual solid precipitation at this site is on the order of 30-40 mm snow water equivalent. A typical sublimation of 10-20% leads to net annual accumulation of around 25-35 mm snow water equivalent. The temperature always remains below -30° C and therefore, no melting occurs. Because of the highly stable conditions of this test site it is used as external cold calibration target for spaceborne radiometers (Njoku et al., 2004). In the present study, the range of vertically and horizontally polarized

brightness temperatures, T_v and T_h, and their annual variability were examined and compared with those of SMMR and AMSR-E at similar frequencies. Usually, snow morphological characteristics, such as grain size, density and correlation length also vary with location based on temperature and snow deposition, which in turn are influenced topography, slope and katabatic winds (Furukawa et al., 1996).

Table 5.1 Coordinates of selected study area location

Area Name	Short Notations	Location Lat: Lon:	Altitude (meters)
Dome Concordia station	Dome C	-74.85 to –75.35 122.0 to 124.0	~ 3260
Lake Vostok	LVT	-76.28 to -77.00 104.0 to 105.0	~ 3500
Between Wilkes Land and Terre Adelie	Study Area 3 (SA3)	-75.5 to -74.5 128.0 to 130.0	~ 3100
Queen Mary Land	QML	-74.5 to -73.5 95.0 to 97.5	~ 3500
Near Pionerskaya Russian Station	PRS	-70.8 to -70 97.0 to 99.5	~ 2500
Wilkes Land	WL	-70.8 to -70.0 120.0 to 122.5	~ 2400
Terre Adelie	TeAd	-70.5 to -69.5 134.0 to 136.0	~ 2500

Figure 5.1(b) shows the direction of the local topographic slope with respect to north. In most parts of Antarctica the surface is influenced by persistent winds, called katabatic winds, which maintain speed and direction over weeks. Katabatic winds produce the periodic wave-like features of snow called satrugi. All these factors contribute to the azimuthal anisotropy of the surface features of the Antarctic ice sheet (Furukawa et al., 1996; Furukawa and Young, 1997). In this study, we use seven area across Antarctica (Figure 5.1(a)) in order to develop an initial understanding of the U and V azimuthal response in Sections 5.2 to 5.5. The areas include flat topography, i.e. Dome C and

Lake Vostok, anisotropic surface topography, and sastrugi, i.e. Study
Areas 3, Wilkes Land, Terre Adelie, areas near the Russian station
Pionerskaya and Queen Maud Land. Lake Vostok is 250 km long by
50 km wide and located at 77 S and 105 E near the Russian station
Vostok. The selected study area of 50 x 50 km lies on the nearly 4000
meter thick ice sheet over a liquid lake and provides flat surface ice
topography over the scale of the WindSat footprint. Table 5.1 shows
the coordinates of the locations and their altitudes.

5.2 T_v and T_h analysis

The T_v and T_h observations of different radiometers, such as AMSR-
E and SMMR at similar frequencies as those of WindSat, have been
investigated over different locations in Antarctica (Njoku et al., 2004;
Surdyk and Fily, 1995). The observations at different frequencies are
utilized to estimate quantities such as the temperature and emissivity
of different layers of the snow firn (Ulaby et al., 1986).

   This section verifies the scale and frequency response of WindSat
measured T_v and T_h brightness temperatures over the Antarctic ice
sheet by comparing their behavior with previous studies. Figures 5.2
and 5.3 show the time series of T_v and T_h for Dome C and Wilkes Land.
Surface temperatures measured by automated weather station (AWS)
are also plotted in Figure 5.2 to show the correlation. At the high
altitudes of Dome C there is little precipitation and low wind speeds,
which keeps the surface flat throughout the year, while at Wilkes
Land the snow deposition is higher due to precipitation. However, in
summer all the deposited snow is blown to lower altitude areas, which
results in a snow free ice sheet at the selected location in Wilkes
Land (Goodwin, 1990). This allows the comparison of T_v and T_h over
climatically different areas of Antarctica.

   The seasonal temperature cycle is apparent in both figures and is
most pronounced at 37 GHz. The brightness temperature varies over
the range of ~30 K at 37 GHz from Austral winter (peaks at June
to July) to Austral summer (peaks at December to January). The
seasonal thermal variability is smallest at 6.8 GHz. This is due to
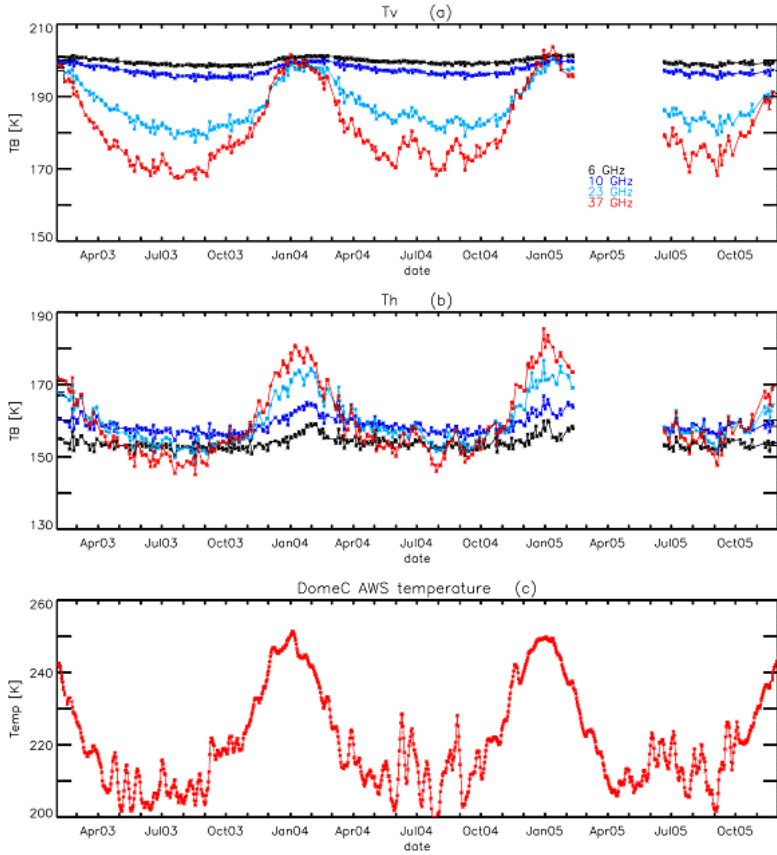
Figure 5.2: Time series of T_v and T_h at 6.8, 10.7, 23.8 and 37 GHz plotted from Feb 2003 to Nov. 2005, for the study area of Dome C. The automated weather station (AWS) measured temperature is plotted together to demonstrate the thermal dependency of these channels.
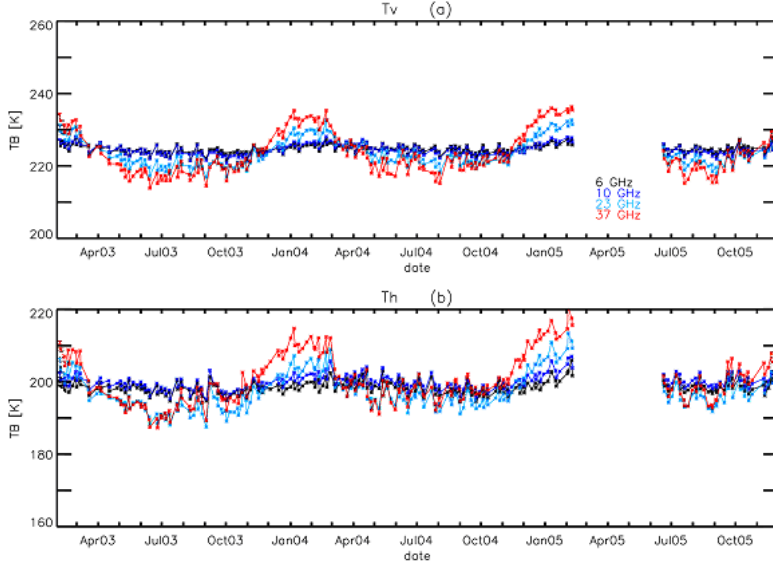
Figure 5.3: Time series of T_v and T_h at 6.8, 10.7, 23.8 and 37 GHz plotted from Feb 2003 to Nov. 2005, for the study area of Wilkes Land.

the difference between the penetration depths at the two frequencies and to the fact that the physical properties of the ice sheet below 10 meters are nearly constant in time. In a recent paper (Macelloni et al., 2007) model analysis demonstrated that the penetration depth in the Dome C area ranges from 20 m at 6.8 GHz to 2 m at 37 GHz. Therefore, the temperature cycle of AWS measurements agrees qualitatively with the 37 GHz measurements, as shown in Figure 5.2. However, the magnitude of the seasonal variation is about 55 K. The lower seasonal variation is caused by the less pronounced seasonal cycle at the penetration depth (about 2 m) and by the emissivity of the snow which is less than unity. The penetration depth is also affected by the snow morphological properties, such as grain size and density. Unlike Dome C, Wilkes Land exhibits higher fluctuations in the daily averaged T_B values (Figure 5.3). This is because the different footprints are at different locations and average altitudes within the test region (Njoku et al., 2004).
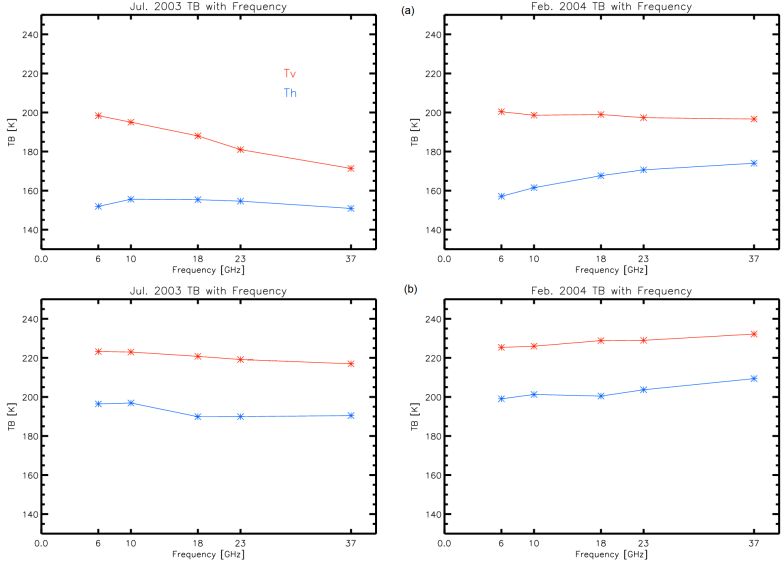
Figure 5.4: Average brightness temperature as a function of frequency of the WindSat measured T_v and T_h for Dome C (top) and for Wilkes Land (bottom).

The average brightness temperatures as a function of frequency for the two areas for winter and summer months are shown in Figure 5.4. For Dome C, T_v decreases and T_h remains almost constant during winter, while during summer T_v remains constant and T_h increases with frequency. For Wilkes Land, T_v and T_h decrease slightly with frequency during winter and increase slightly during summer. The difference between the T_v and T_h spectral behaviors is due to the difference between the snow density and grain size at the two locations (Surdyk and Fily, 1995). These types of spectral responses can be explained by the emissivities of different snow types (Surdyk and Fily, 1995). For the snow grain size of 0.5 mm the T_v and T_h decreases with frequency, while for size of 2 mm they increase. At Dome C the grain size is on the order of 2 mm whereas at Wilkes Land it is on the order of 0.5 mm. The details of spectral response can be found in (Surdyk and Fily, 1995). The WindSat measured T_v and T_h signals, their scale

and annual variability are in good agreement with previous studies, conducted using SMMR (Surdyk, 2002) and AMSR-E (Njoku et al., 2004; Macelloni et al., 2007) data.

5.3 Azimuthal anisotropy in U and V

The anisotropic surfaces give rise to non-zero U and V signals. For sea surfaces the wind generated waves cause this anisotropy, while for land the topography at different roughness scales and vegetation structures are responsible (Narvekar et al., 2007). In this section the anisotropic signal observed in U and V over the Antarctic ice sheet is investigated.

5.3.1 U component

To study the extent to which the higher Stokes components depend on the snow surface structure, the flat areas of Dome C and Lake Vostok and the structured areas of Wilkes Land (WL) and Study Area 3 (SA3) were selected for the initial azimuthal analysis. Figures 5.5a and 5.5b show the azimuthal distribution of 10.7 and 37 GHz U observations for the entire month of February 2004 for all four areas. Different colors indicate the mode of the measurements.

Over most parts of Antarctica, the climatic and surface geophysical properties typically remain similar over several weeks (Long and Drinkwater, 2000), unless there is a snow fall event. This mainly occurs at low altitudes near the coast in winter (Turner et al., 1999). If we assume this to be true then we are able to combine multiple passes over several days. The solid line indicates the fit of a second harmonic sine function to the variations of data points with the radiometer azimuth angle. These harmonic curves will be discussed in depth in Section 5.4. A clear anisotropic signal is apparent from the plots in the Figures 5.5a and 5.5b. The maximum anisotropic signal for Dome C and Lake Vostok (LVT) is less than 2 K, whereas for WL and SA3 the maximum is around 4 K. At 37 GHz the signal for Dome C and LVT is much lower (>1K). This can be explained by
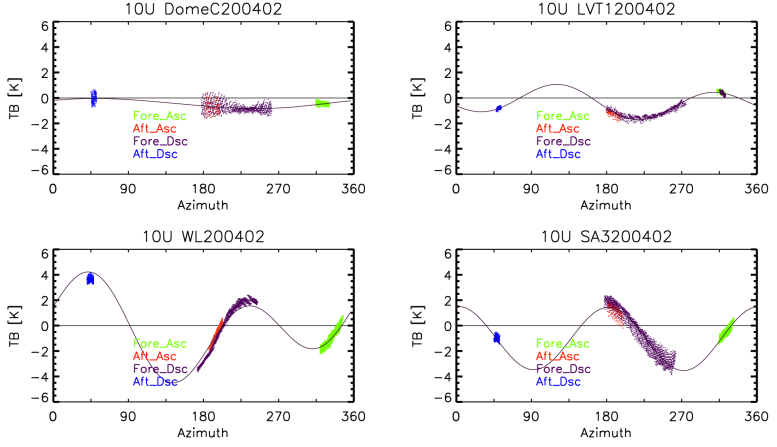
(a)
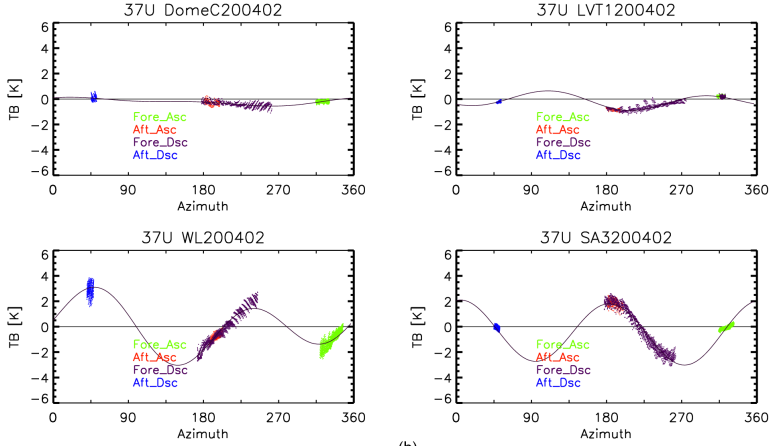
(b)

Figure 5.5: The azimuthal distribution of the (a) 10.7 GHz and (b) 37 GHy
U observations of February 2004, top left for Dome C, top right for Lake
Vostok, bottom left Wilkes Land and bottom right for Study Area 3. The
curves fitted is the second harmonic sine function of azimuth angle.

the sastrugies present at WL and SA3. These contribute to a higher magnitude signal than that observed over the flat surfaces of Dome C and LVT. The magnitude of the U component observed is higher than that observed over sea or land surfaces where it rarely exceeds 2 K (Yueh et al., 2006; Narvekar et al., 2007). However, the magnitude of U in Figures 5.5a and 5.5b, for the anisotropic areas of WL and SA3, are of the order of 4 K. The snow and ice microphysical characteristics are different from those of sea and land surfaces (Ulaby et al., 1986). The microwave emissivities of the snow and ice targets are high ($\sim$0.9) while the ocean exhibits a low value. Moreover, snow consists of a large number of grains acting as scatterers. Under thermal equilibrium the emissivity is related to volume scattering (Tsang et al., 1985). Since U is primarily a function of scattering, this could be one possible reason for the higher magnitude of the U component (and also V signal, discussed later) as compared to open ocean and land. Differences were observed between the 10.7 and 37 GHz signatures of Dome C (top left plots of Figure 5.5a and 5.5b).

The 10.7 GHz fore swath descending observations have a higher spread around the second harmonic curve than those at 37 GHz. The high scatter in the 10.7 U of Dome C is likely to be caused by volume scattering, which is little at 37 GHz due to the lower penetration depth. Due to the low average wind speeds (4 m/sec) and the low deposition rate ($\sim$3 cm p.a.) the snow surface is flat at Dome C as compared to LVT, which has snow drifts generated by surface winds, however, these are much smaller in magnitude as compared to the sastrugi observed at WL and SA3. This explains why the 37 GHz U observations of Dome C show minimal modulation with azimuth angle when compared to the other regions. In Sections 5.4 and 5.5, the seasonal and spatial variability of the second harmonic coefficients of the U component will be investigated.

5.3.2 V Component

Figures 5.6a and 5.6b show the 10.7 and 37 GHz V components plotted as a function of azimuth angle. All plots show a clear anisotropic sig-
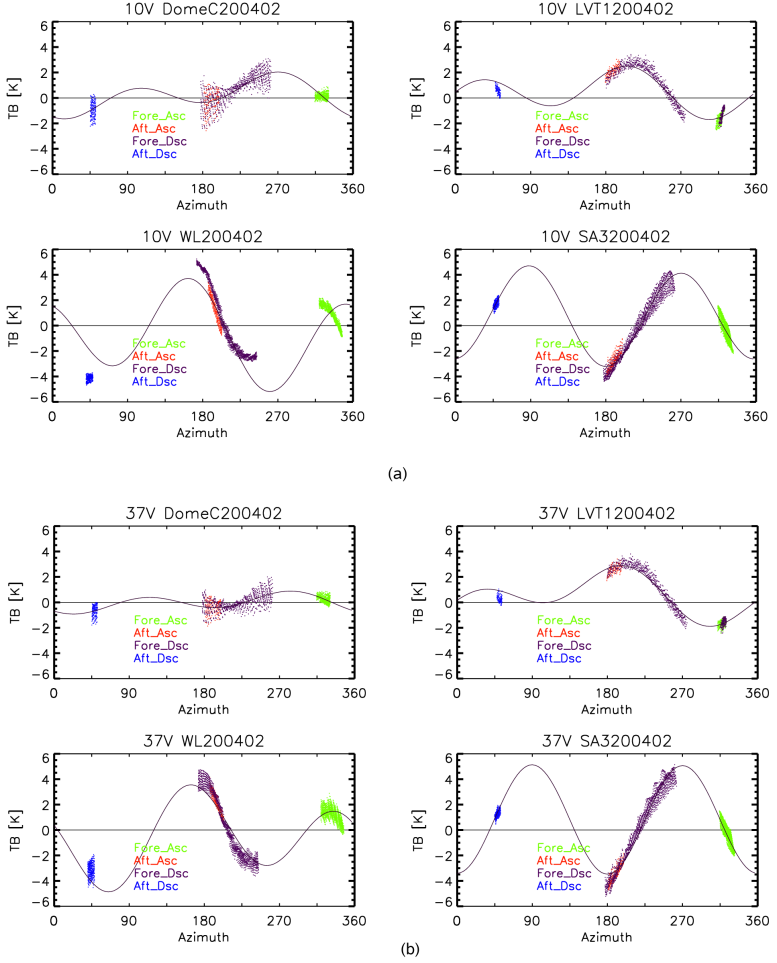
Figure 5.6: The azimuthal distribution of the (a) 10.7 GHz and (b) 37 GHz *V* observations of February 2004, top left for Dome C, top right for Lake Vostok, bottom left Wilkes Land and bottom right for Study area 3. The curves fitted are the second harmonic sine function of azimuth angle.

nal, with variations larger than those observed for the U component. For the nearly isotropic regions, Dome C and LVT, the magnitude at both frequencies is about 2 K. For WL and SA3, which have a pronounced terrain slope and sastrugi, the magnitude reaches 4 K. This is much higher than the V signal over open ocean where it is only around to 0.5 K (Yueh et al., 2006). The V signal can be explained by second or higher order scattering that produces coherent signals with phase shifts on the order of the wavelength (Yueh, 1997). While the first order scattering produces incoherent waves, the higher orders produce coherently scattered waves. For the sea surface the higher order scattering is generated by small ripples as well as from the adjacent large gravity waves. A non-zero V signal can be modeled with wave scattering and small slope approximation methods (Yueh, 1997).

In the case of snow, absorption and scattering primarily depend upon parameters such as snow grain size and density, which usually vary with depth (Tsang et al., 1985; Ulaby et al., 1986). The vertical profile of these parameters is typically modeled as horizontally stratified layers (Surdyk, 2002). The difference between the layers with different snow morphological properties is called the correlation length. The higher order scattering from the different layers and from the snow surface structures, such as sastrugi and snow dunes, causes the coherent signal (Narvekar et al., 2007b). The azimuthal dependence of the V signal indicates a directional preference of the higher order scattering processes. In regions of strong terrain slope and sastrugies, such as WL, the azimuthal preference of the V signal is clearly pronounced. The azimuthal dependence of the V signal of Dome C shows a large scatter around the harmonic fit (Figure 5.6a). Our explanation of this is that within each single WindSat footprint the azimuthal structures are coherent enough to generate a non zero V signal, whereas from one footprint to another in the Dome C region the prevailing orientation of the scattering structure may vary. In contrast, within each of the other three regions the azimuthal orientation of the scattering structure is nearly constant, producing a well defined variation with azimuth. At 10.7 GHz V observations over WL, the second harmonic function do not fit, this may be due to the additional effects of volume scattering involved at this frequency.

5.4 Modelling azimuthal anisotropic signal

Models and aircraft observations of the sea surface have shown a second harmonic sinusoidal dependency of the U and V components on the azimuth look angle (Yueh, 1997). These observations have also shown a good agreement with the scatterometer results obtained over sea surfaces, since U and V measured by radiometers and the backscatter coefficient measured by scatterometers both depend primarily on the geometric structural properties of the sea surface. There have also been some scatterometer studies over the Antarctic ice sheet using the NASA SCATterometer (NSCAT) and ERS SCATterometer (ESCAT) (Long and Drinkwater, 2000; Bingham and Drinkwater, 2000). Furukawa and Young (1997) have also compared the amplitude of ESCAT backscattering coefficient with ground observations of different scaled snow and ice features obatined from the field experiments. The study described in (Long and Drinkwater, 2000) utilized a second order harmonic cosine functions to estimate the orientation of the snow surface features, such as sastrugi and the topographic slope. In the present study a second harmonic sine function of the relative azimuth angle together with an additional constant term is used to empirically fit:

$$U = U_1 sin(\varphi_{rel} + \varphi_{ph}) + U_2 sin2(\varphi_{rel} + \varphi_{ph}) + U_3$$

$$V = V_1 sin(\varphi_{rel} + \varphi_{ph}) + V_2 sin2(\varphi_{rel} + \varphi_{ph}) + V_3. \qquad (5.1)$$

The relative azimuth angle φ_{rel} is the difference between the direction of the orientation of the snow features and the radiometer azimuth angle: $\varphi_{rel} = \varphi_{struc} - \varphi_{rad}$. In sea surface studies φ_{struc} is the wind direction (Yueh, 1997). An additional constant phase angle φ_{ph} of 90° is added to the azimuthal term in order to facilitate the comparison between the WindSat and scatterometer results. U_1 and V_1 are the magnitudes of the first harmonic coefficients that describe the up-wind/down-wind asymmetry, while U_2 and V_2 describe the up-wind/crosswind asymmetry. The constant terms U_3 and V_3 define the offset in the fit from the 0 K average.

Table 5.2   Estimated orientations from WindSat and Nscat data

Short notations	φ_{struc} (in °)					err/U_2			
	WindSat U				NSCAT vv	WindSat U			
	Jul. 03		Feb. 04		Sep. 96	Jul. 03		Feb. 04	
	10.7 GHz	37 GHz	10.7 GHz	37 GHz	14 GHz	10.7 GHz	37 GHz	10.7 GHz	37 GHz
TeAd	144°	161°	145°	141°	~135°	0.28	0.44	0.16	0.17
PRS	131°	138°	127°	116°	~120°	0.53	0.39	0.13	0.76
SA3	142°	127°	141°	139°	~150°	0.55	0.57	0.47	0.13
WL	100°	100°	95°	99°	~100°	0.30	0.41	0.14	0.18
QML	20°	112°	107°	126°	~100°	3.06	0.23	0.22	0.56
Dome C	158°	156°	152°	141°	~153°	0.85	0.22	11.1	1.00
LVT	169°	162°	170°	159°	~175°	0.46	0.35	0.14	0.24

The second harmonic fits for the WindSat data are shown as solid lines in Figures 5.5a, 5.5b, 5.6a and 5.6b. The coefficients U_1, U_2, U_3, V_1, V_2, V_3 in K, and φ_{struc} (in °) have been estimated from the data points. Due to the periodic nature of sastrugi, similar to that of waves observed over a sea surface, the second harmonic sine function fits the data well. The quantities 'err' and 'err/U_2' describe the quality of the fit. 'err' is the root mean square error of the fit in K. Values near or higher than one for err/U_2 indicate that the standard deviation is higher than the estimated second harmonic coefficient. The estimated quantities are shown in Table 5.2.

We compared the estimated orientation angles with the previous scatterometer results (Long and Drinkwater, 2000) for selected study areas. To account for the seasonal influence on the retrievals, the two months of July 2003 and February 2004 with contrasting climate conditions were selected. Over WL the direction of the derived streamline

is related to the orientation of sastrugi (Long and Drinkwater, 2000). The direction of orientation estimated over WL using the second harmonic fitting of azimuth for the 10.7 GHz U observations is 95° and 100°, for July 2003 and February 2004 respectively, with respect to North. Both results agree well with the scatterometer derived direction of the stream line of $\sim 100°$ (Long and Drinkwater, 2000). Similar comparisons were made for the other areas (Table 5.2). Good agreement was found for all the cases except for winter (July 2003) at Queen Mary Land (QML). As the rms error of this fit is three times the value of U_2, this direction estimation is of little significance, indicating a low prevailing directionality of the observed surface structures. Since volume scattering plays a critical role in the signal observed at 10.7 GHz, during winter the presence of a thick layer of snow could form a medium with varying orientations. Also, changes over time could explain the discrepancy between the NSCAT and WindSat observations because they are from different years. In a recent theoretical study (Xu et al., 2007), a electromagnetic modeling approach was presented that considered snow and ice surface anisotropy along with the contribution from the subsurface layers, in explaining the polarimetric emission over snow. In most of the cases, the estimated orientation of 37 GHz U were different for July 2003 and February 2004, which were different from the 10.7 GHz U and NSCAT estimations. The 37 GHz U observations are from the topmost layers and, therefore, the estimated orientation represents the snow surface structures, such as snow drift caused due to the surface winds. In order to obtain a better perspective of the estimated orientation and to facilitate its comparison with the scatterometer results, the fit will be extended over the entire Antarctica in Section 5.6.

5.5 Seasonal variability

Snow fall changes the surface and volume snow properties such as density and correlation length (Bingham and Drinkwater, 2000). The snowfall occurs mostly in winter and sometimes in spring. This modulates the Antarctic snow morphological properties with the seasons.

To investigate in detail the seasonal variability of the U and V observations, the study area of Wilkes Land was selected because this is one of the locations for which the time series of the ESCAT backscattering coefficients was investigated by Bingham and Drinkwater (2000).
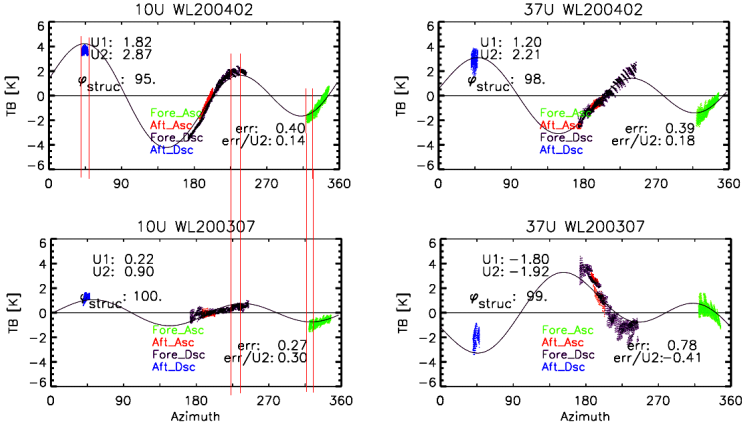

Figure 5.7: Selection of the azimuth angle range in fore ascending ($320° \pm 10°$) and fore descending ($225° \pm 10°$) with low variability with azimuth angle for preparing a time series of Wilkes Land, top panel corresponds to the 10.7 and 37 GHz U observations of February 2004 and lower panel corresponds to observations of July 2003.

The time series was generated using daily observations averaged over two small azimuth angle ranges indicated in Figure 5.7. The upper panel shows the azimuthal distribution of the 10.7 and 37 GHz U components for February 2004 and lower panel shows the same for July 2003. The brightness temperatures at angles near $225°$ (fore descending), $320°$ (fore ascending) and $45°$ (aft descending) show the lower variations with azimuth angle. Therefore, the azimuthal ranges $225°$ to $240°$ for ascending and $320°$ to $335°$ for descending overpasses were selected for averaging.

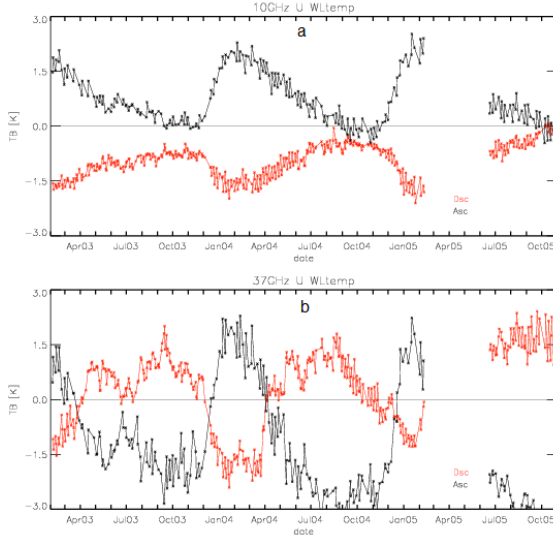These correspond to nearly perpendicular azimuth directions. There-

Figure 5.8: Time series of 10.7 GHz (a) and 37 GHz (b) U components over Wilkes Land, February 2003 to November 2005.

fore, the larger difference between ascending and descending U values corresponds to higher anisotropic signals. If the difference is smaller or zero, then the target shows a lower anisotropy.

Figure 5.8 compares the time series of 10.7 GHz and 37 GHz U. The WindSat data were averaged for each day over the above indicated azimuth ranges at Wilkes Land. The time series of T_v (Figure 5.3) helps in recognizing the seasonal cycle. In Figure 5.8a, the 10.7 GHz U observations show high anisotropy between January and April (summer) and minimum anisotropy between July and September (winter). This behavior might be explained by the fact that the snow deposition rate in Wilkes Land is higher during winter (Goodwin, 1990). The newly deposited snow has a different density and grain size from the previous snow cover, which change with seasons (Turner et al., 1999; Goodwin, 1990; Massom et al., 2004). During summer, most of the snow will have migrated from this area to low altitude coastal areas
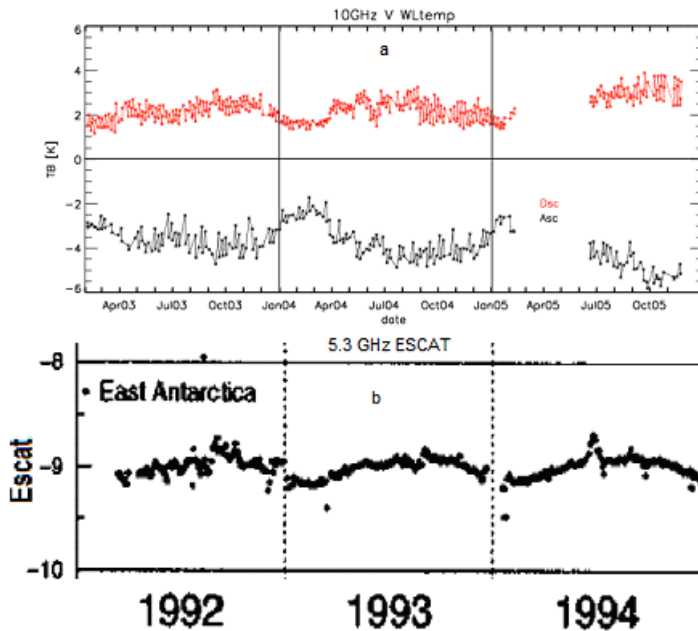
Figure 5.9: Time series of 10.7 GHz V component over Wilkes Land, February 2003 to November 2005, plotted previously made time series of ESCAT measured backscattering coefficient (adopted from (Bingham and Drinkwater, 2000))

due to katabatic winds (Goodwin, 1990). This significantly decreases the volume scattering at 10.7 GHz (Figure 5.8a). This could be an explanation for the sharp increase in the azimuthal anisotropy as the summer approaches because the anisotropic signal is expected to be more pronounced near the surface (from where the signal in summer stems) than in the depth. The 37 GHz U response pattern shown in Figure 5.8b is similar in shape to the 10 GHz U signal but the dynamic range of both ascending and descending data is doubled from about 2 K to 4 K. Moreover, the curves for 37 GHz (Figure 5.8b) are shifted by a constant offset, compared to 10.7 GHz (Figure 5.8a).

The months of February and September correspond to the maximum and minimum directional signals, respectively for 10.7 GHz. However, for 37 GHz both months correspond to maximums, but with opposite T_B sign. Moreover, the 37 GHz U signal shows a much more pronounced variation from day to day, on the order of 1 K, in contrast to the smoother 10.7 GHz U signal, with variations of typically 0.5 K. The higher daily and seasonal variations of the 37 GHz signal compared to the 10.7 GHz U signal can be explained by the lower penetration depth at 37 GHz which would be impacted more by seasonal temperature and wind.

In addition, wind speed is higher during the winter (Van Den Broeke et al., 1997), which leads to an orientation of the snow features such as sastrugi in the prevailing direction. Figure 5.9 shows the time series of the 10.7 GHz V components for the study area of Wilkes Land for the same azimuth angle ranges as discussed previously. A seasonal trend is apparent for both azimuth ranges. In contrast to the U component (Figure 5.8a, b), the absolute maxima in the V component (Figure 5.9a) occur in winter and the absolute minima in summer. The annual cycle observed agrees well with that observed in the ESCAT data (Figure 5.9b) (Bingham and Drinkwater, 2000). The backscattering coefficient increases during winter due to volume scattering (Bingham and Drinkwater, 2000). As discussed in section 5.3.2, the V signal is assumed to be caused by higher order scattering. This would explain the higher magnitude V signal observed during winter.

5.6 Extending harmonic fit over entire continent

In order to prepare maps of estimated coefficients and to study their seasonal variability, the data for the first 15 days of July 2003 (Austral winter) and the month of February 2004 (summer) were analyzed. The data from the WindSat passes over 15 days were first sampled into grid cells of 0.25° x 0.25°. The second harmonic fit (Equation 5.1) was applied to each grid cell and the maps of the estimated parameters, i.e.

φ_{struc}, U_1,U_2,V_1 and V_2 are presented and discussed in the following subsections.

5.6.1 Orientation of the snow features

Figure 5.10 show the maps of the estimated φ_{struc} using the WindSat 10.7 GHz and 37 GHz U observations for July 2003 (Austral winter) and February 2004 (Austral summer). The middle panel shows the orientation angle estimated previously using scatterometer observations from ESCAT and NSCAT (Long and Drinkwater, 2000) based on the data from September 1996. The scale of the WindSat derived maps is reverse compared to the scatterometer results because the phase angle φ_{ph} of 90° is added in the model of Equation (5.1). We found that results obtained by adding this phase angle facilitate the comparison between WindSat and NSCAT results. The results obtained from the NSCAT observations at 14 GHz agree well with WindSat results at 10.7 GHz, especially over Queen Maud Land, Kemp Land, Terre Adelie and Wilkes Land. Minimal differences were observed between the orientation derived for winter (July 2003) and summer (February 2004 at 10.7 GHz. As noted earlier, the 10.7 GHz data are responding to deeper/subsurface layers. Their orientation changes very little with the seasons and snow drift, and dunes at the surface have limited impact on the estimated orientation (Figure 5.10a). The orientation estimated from the ESCAT observations of September 1996 (5.3 GHz) corresponds to even lower depths than 10.7 or 14 GHz, and therefore, φ_{struc} would be expected to vary even less as observed in Figure 5.10b. The maps of obtained from the 37 GHz observations (Figure 5.10c) exhibit variations at smaller horizontal scales than the 10.7 GHz maps of Figure 5.10a, and the map of winter data (Figure 5.10c left) varies at smaller scales than that of summer (Figure 5.10c right). The orientation angle estimated using 37 GHz is influenced by the surface features, which in turn are driven by the wind speed and snow deposition. Our interpretation of these results is that the reduced feature scale in summer (Figure 5.10c right) reflects the high temperatures,

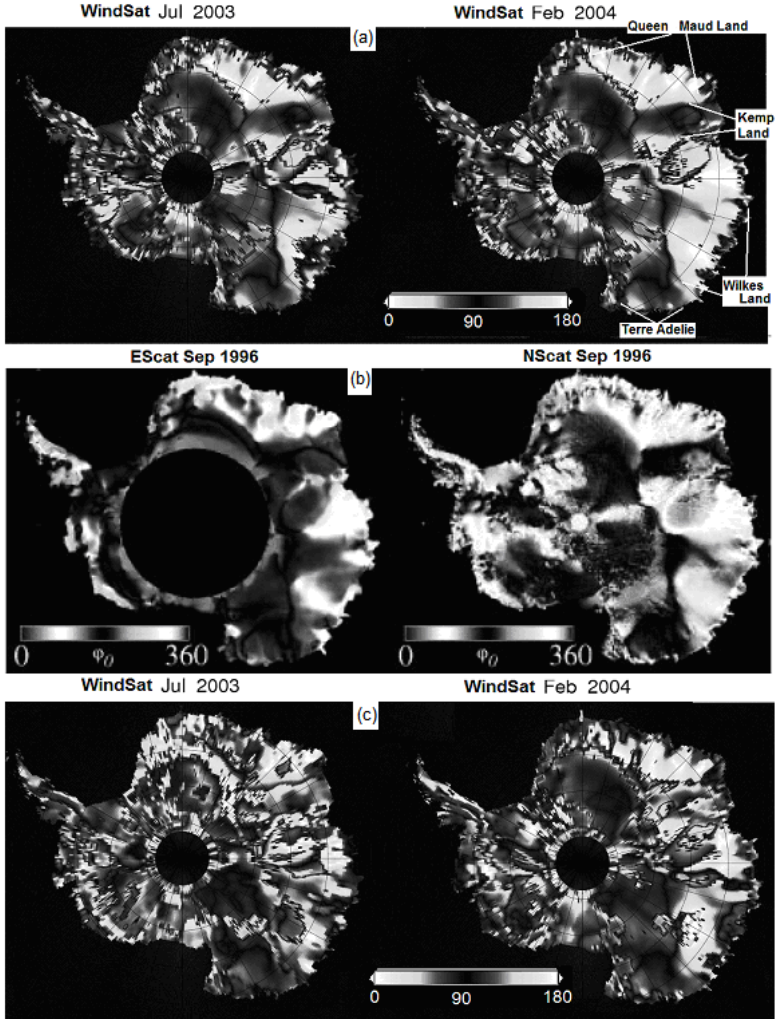Figure 5.10: Estimated φ_{struc} using WindSat 10.7 GHz and 37 GHz U observation of July 2003 and February 2004 (a) and (c) respectively, compared with the previous results from ESCAT and NSCAT (b) (adopted from (Long and Drinkwater, 2000)).

low snow cover and generally lower wind speeds in summer as com-
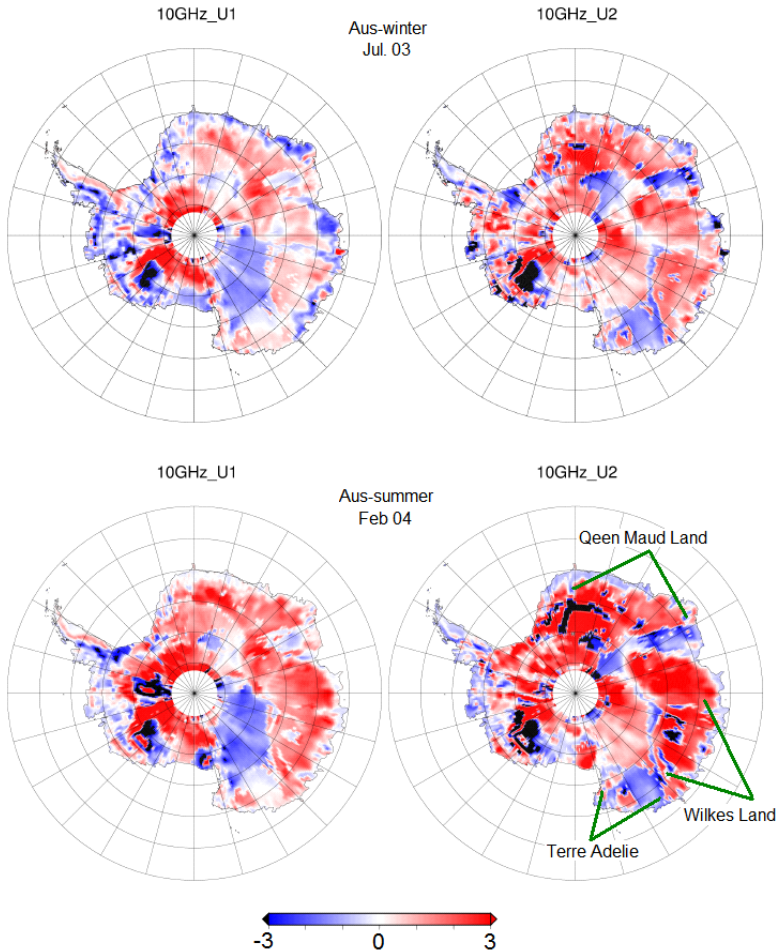pared to winter conditions (Figure 5.10c left).

Figure 5.11: Antarctic maps of estimated U_1 and U_2 coefficients using 10.7
GHz U observation for July 2003 (top) and February 2004 (bottom).

5.6.2 First and second harmonic coefficient

Figure 5.11 shows Antarctica maps of the parameters U_1 and U_2 at 10.7 GHz for winter (July 2003) and summer (February 2004). Both U_1 and U_2 show correlation with the surface topographic slope (Figure 5.1b). In the U_1 maps (top and bottom left), the ridge of the mountain ranges is apparent with values close to 0 K. For east Antarctica, the ridge acts as a separator of positive and negative U_1 value. Moreover, an interesting difference was observed between the U_1 maps of July 2003 and February 2004. The coastal areas extending from Queen Maud Land to Wilkes Land, show negative U_1 value in winter (Jul. 03), which then approaches 0K (white) during summer (Feb. 04). Several studies such as (Massom et al., 2004) have reported that the coastal areas receive a high amount of snow fall, annually ($\sim$ 500 kg/m2). This can have a significant volume scattering effect at 10.7 GHz. During summer the increase in moisture content reduces the penetration depth, which would result in volume scattering and a U_1 signal at 10.7 GHz.

Over the regions of Queen Maud Land and Wilkes Land, the positive magnitude of U_1 and U_2 increases in summer. In the interior continent where no summer melt occurs, the second order coefficient U_2 is generally higher in magnitude than the first order coefficient U_1 (Figure 5.11). The parameters V_1 and V_2 estimated at 10.7 GHz are shown in Figure 5.12. The topographic features of near zero values near the mountain ridges as found in the U_1 and U_2 maps at 10.7 GHz in Figure 5.11 are also visible in the V_1 and V_2 (Figure 5.12). Similar to the U components of Figure 5.11, also in the V components of Figure 5.12, the V_2 coefficients are generally higher than the V_1 component. However, in contrast to the U_1 and U_2 values of Figure 5.11, the magnitude of V_1 and V_2 is higher during winter than during summer (Figure 5.12). We attribute this to volume scattering and higher order scattering. During winter the snow cover is usually dry and, therefore, at 10.7 GHz the subsurface snow layers contribute to scattering. However, during summer the significance of volume scattering decreases. This explains the difference between the magnitudes that occur during the two seasons. Moreover, for the regions of Wilkes
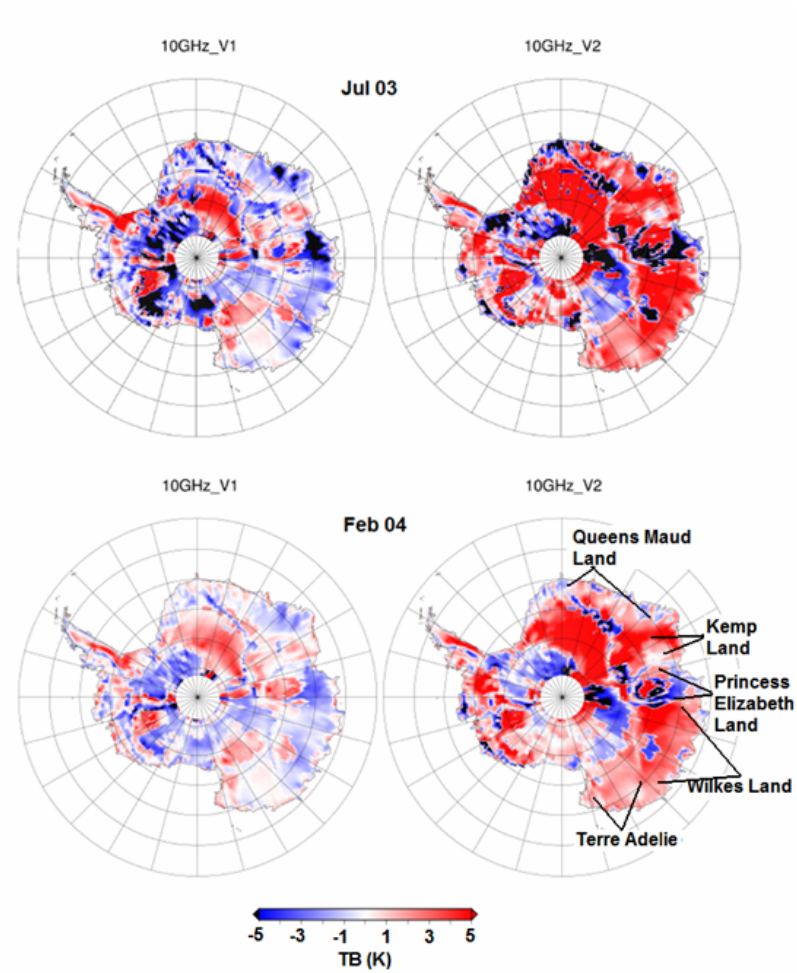
Figure 5.12: Antarctic maps of estimated V_1 and V_2 coefficients using 10.7 GHz V observation for July 2003 (top) and February 2004 (bottom).

Land ($> 74°$ S and $120°$ E) and Terre Adelie ($> 75°$ S and $160°$ E) there is very little differencee. This was also observed for the 10.7 GHz U_1 and U_2 components in Figure 5.11. The signals over west Antarctica were not considered in this analysis due to the complex surface conditions resulting from the mixture of surface topography, sastrugi and erosional features. In the interior Antarctic regions Wilkes Land and Terre Adelie, the seasonal variability is lower. Dome C is one of the areas in this region that has less seasonal variability in both its climatic conditions and the higher Stokes components. This shows the sensitivity of the U_1 at 10.7 GHz for snow deposition. The coefficients estimated using 37 GHz U and V data have lower magnitude for U_1 and V_1 than U_2 and V_2, respectively, for both summer and winter seasons. This was similar to those of 10.7 GHz presented previously. However, the magnitude of these coefficients remains highly variable throughout the year, which can be easily seen from Figure 5.8c.

5.7 Conclusions

Fully polarimetric brightness temperature observations from WindSat were studied for the Antarctic ice sheet. The T_v and T_h brightness temperature ranges were found to be consistent with previous studies and, therefore, used as references. The WindSat observations at 10.7 and 37 GHz were utilized for investigating the azimuthal dependency of the U and V components over the Antarctic ice sheet. The seasonal variation in the magnitude of the U and V was studied based on earlier scatterometer studies. Results showed that the U and V signals depended on the snow deposition rate and other morphological properties. A second order harmonic sine function was fitted to the U and V observations. The first and second harmonic coefficients along with structural direction were estimated. The estimated coefficients and orientation angles showed good agreement with the similar coefficients estimated using scatterometer datasets. From the analyses, a consistent pattern of behavior emerged for the 10.7 GHz observations: under winter conditions, the high contribution of multiple volume scattering causes a high (Figure 5.9a) and regionally

variable (Figure 5.12) 10.7 GHz V signals as well as high backscattering coefficients (Figure 5.10b), while under summer conditions, the surface scattering prevails, causing high U signals (Figures 5.8b and 5.11). For the 37 GHz channels that do not include contributions fom deeper layers, the contrast between summer and winter observations was less pronounced in magnitude, however the sign of the harmonic fit tended to change between seasons (Figure 5.8c). Scatterometer observations from a previous investigation were related to the passive sensors operating at T_v and T_h for the information of surface thermal properties. However, the fully polarimetric radiometer WindSat measures T_v, T_h along with U and V and, therefore, this study suggests a potential value in providing scattering emission and thermal information from the single sensor package.

6 Passive Polarimetry for Arctic Sea Ice

Here the WindSat data over Arctic sea ice is investigated for the geophysical information content in the polarimetric brightness temperatures. U and V are primary function of the magnitude of roughness, and the angle between the direction of the roughness (i.e. direction of waves) and the radiometer look angle. Moreover, the studies performed over land and over the Antarctic ice sheet have shown the dependency of U and V on the orientation of the surface features (Narvekar et al., 2007; Narvekar et al., 2006). Over land these features include agricultural field rows and sand dunes in the desert. Over the Antarctic ice sheet, these features include snow dunes, so called sastrugi, caused by katabatic winds and structures caused by erosion. However, the polarimetric data over sea ice have attracted little attention until now.

6.1 Spatial variability of U and V

The analysis of the U and V components is carried out for the period of two years, 2003-2004. In order to account for the azimuth dependency of U and V, the range of the radiometer azimuth angle is divided into four quadrants of 90° interval from 0° to 360°. We found that the selected scan angle, , range of -25° to +25° results in no data in the 90° to 180° azimuth angle quadrant. Therefore, only the three quadrants from 0° to 90°, 180° to 270° and 270° to 360° are considered.

The spatial and temporal changes are studied by preparing time series of maps of seven day average for each azimuth quadrant over the entire year 2003. The averages were made in a 0.25° grid. In Narvekar
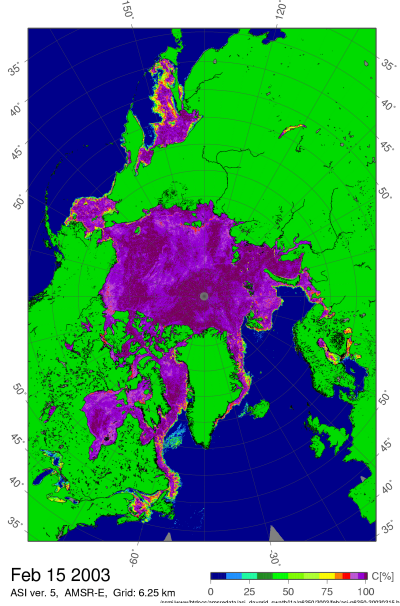
Figure 6.1: Map of ASI Sea ice concentration derived from AMSR-E for
15th Feb 2003.

et al.(2008), the maps of the U and V at 10.7 and 37 GHz from Feb.
2003 to Jan. 2004 are shown. The signals observed are studied using
the reference sea ice concentration maps derived from AMSR-E data.
During most of the year, the 10.7 and 37 GHz U and V signals over sea
ice is below 1 K (Narvekar et al., 2008), which is small as compared
to those observed over ocean surface (2 K) (Yueh et al., 2006), land
surface ($\sim$2 K) (Narvekar et al., 2007) and the Antarctic ice sheet
($\sim$7 K) (Narvekar et al., 2006; Narvekar et al., submitted) and the
Greenland ice sheet (15 K) (Liu and Weng, 2005). The information
about the sea ice edge is extracted from the previously available ra-
diometers operating at dual polarization, such as AMSR-E. During
February 2003, there is high sea ice coverage in the Arctic. Figure 6.1
shows as an example the sea ice concentration on the 15th February
2003. The signal observed at 10.7 GHz V, and 37 GHz U and V dur-
ing this period is nearly zero (Narvekar et al., 2008). The 10.7 GHz
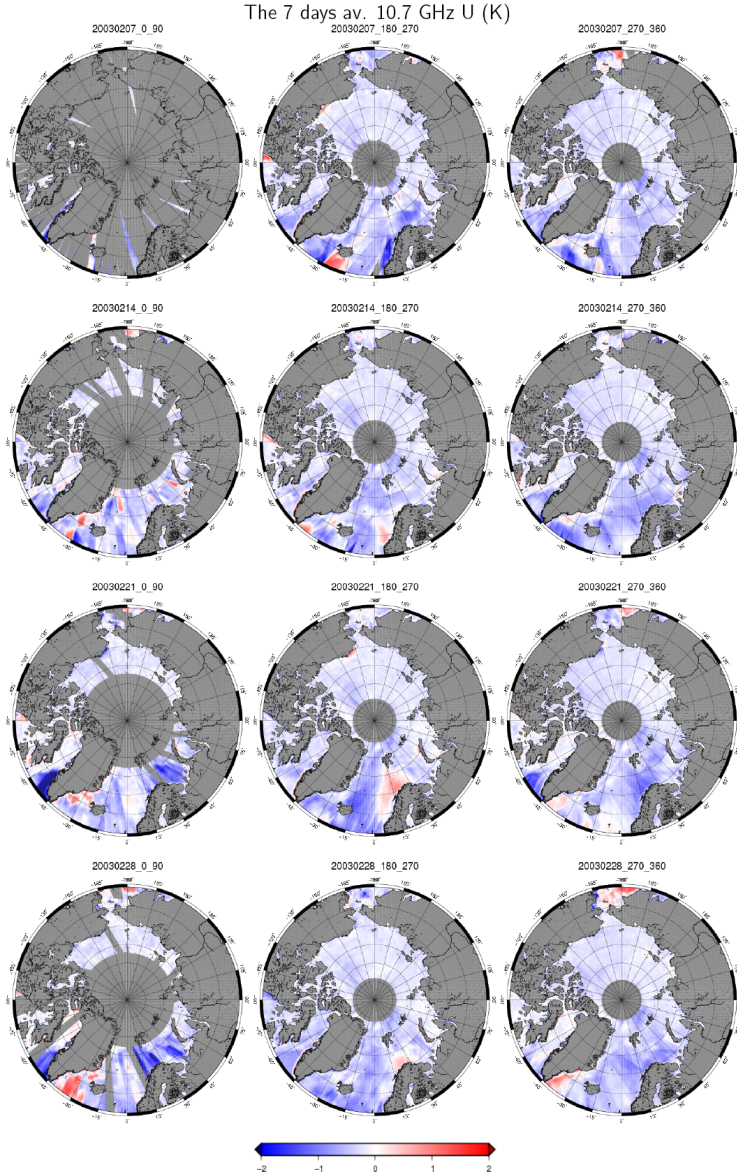U observations are similar, except in the area above North of Franz

Figure 6.2: The 10.7 GHz U component averaged over 7 day for Feb. 2003.
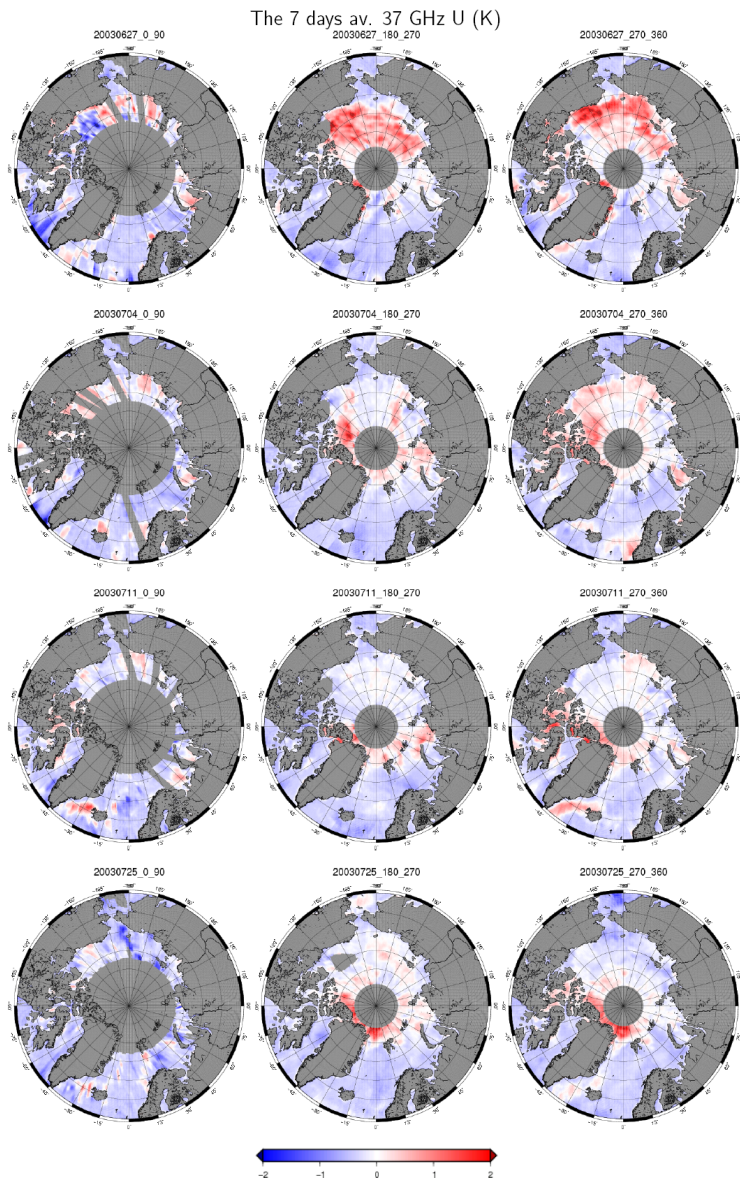
Figure 6.3: The 37 GHz U component averaged over 7 day from end of June to end of July 2003.
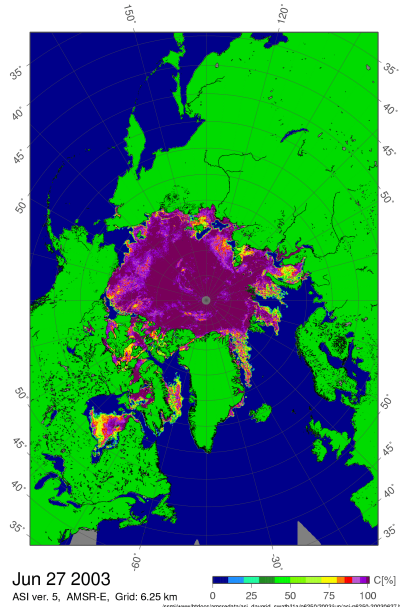
Figure 6.4: Map of ASI sea ice concentrations derived from AMSR-E for 27th June 2003.

Josef Land, where a comparatively high negative signal is apparent in the azimuth quadrant of $270°$ - $360°$, Figure 6.2. However, this signal is still around 1 K.

Moreover, the standard deviation for the WindSat measurements is 0.25 K (Liu and Weng, 2005) and therefore, any signal close to this value are not considered for interpretation here. A similar analysis of the other months was also carried out. During the summer months, parts of the Arctic sea ice show higher U and V signals. As an example, the 37GHz U component shows a high signal over the large area extending from the Beaufort Sea to the New Siberian Islands. The data of June 22nd to 27th show this effect, see the maps of the first row in Figure 6.3. However, signals in the other channels of the same period are low (Narvekar et al., 2008). The melting in the Arctic usually occurs during end of June and early July. Figure 6.4 shows the sea ice concentration on 27th June 2003. It shows that in most of the area the ice concentration is above 90%. The 37 GHz U signal reduces
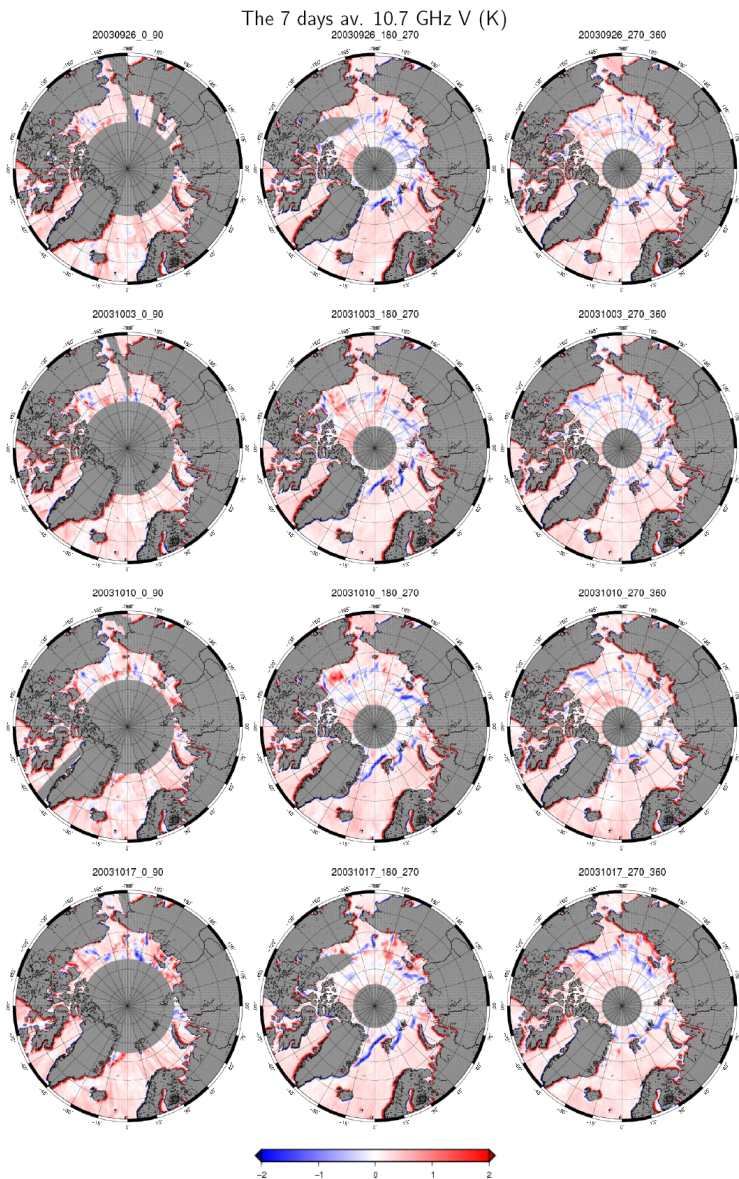
Figure 6.5: The 10.7 GHz V component averaged over 7 day from end of September to end of October 2003.
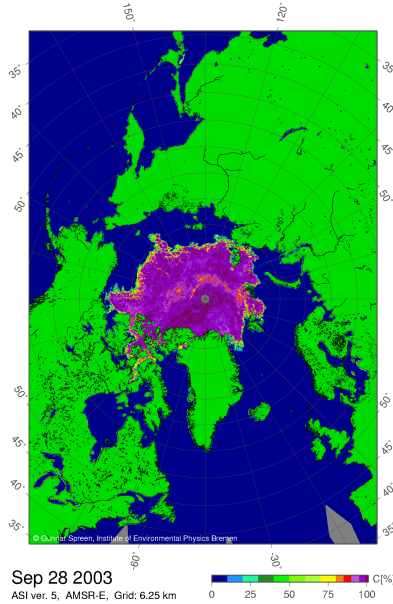
Figure 6.6: Map of ASI sea ice concentrations derived from AMSR-E for 28th Sep 2003.

considerably during the next 7 days (Figure 6.3). Another region of high U signal occurs in the map of 25th July, at 85° latitude north of Greenland (last row of Figure 6.3). This signal is also reduced in the next seven day averaged maps (Narvekar et al., 2008).

Only the 37 GHz U has shown a high signal over the closed ice pack during short periods in the summer months, while the other components remain below 1 K. Another feature of higher Stokes components emerges from the 10.7 GHz V signal from the entire analysis. Over the ice edge there is a clear 10.7 GHz V signal of typically 6 K (Figure 6.5), as we see from the comparison with the ice concentration maps of AMSR-E (Figure 6.6). This effect is not pronounced at 10.7 GHz U and also not at 37 GHz U and V. A global 10.7 GHz V data analysis has shown a high signal also over coastlines. For sea surface applications, a filter is applied over the coastlines so that this data is not used for the wind vector retrieval (Gaiser et al., 2004).

Figure 6.7: The 37 GHz U maps of $180°$ to $270°$ and $270°$ to $360°$ azimuth quadrants compared with ECMWF near surface air temperature map, June 03 to June 16, 2003.
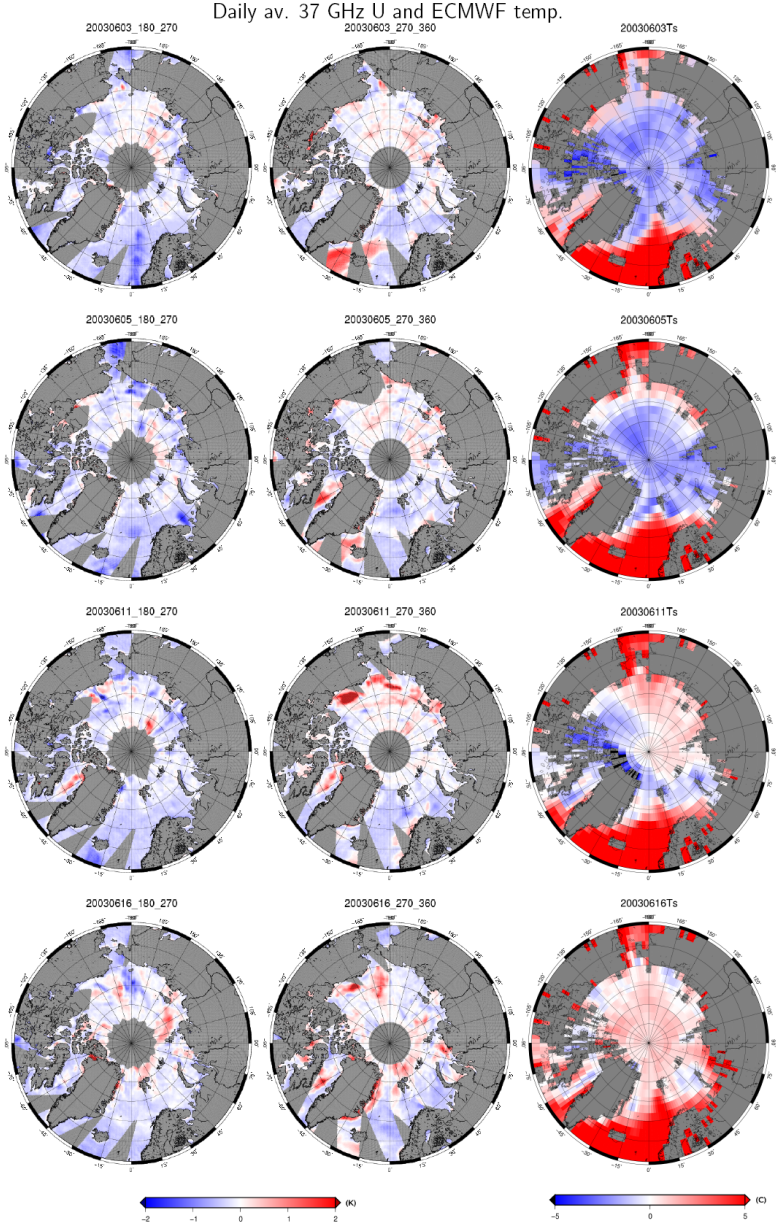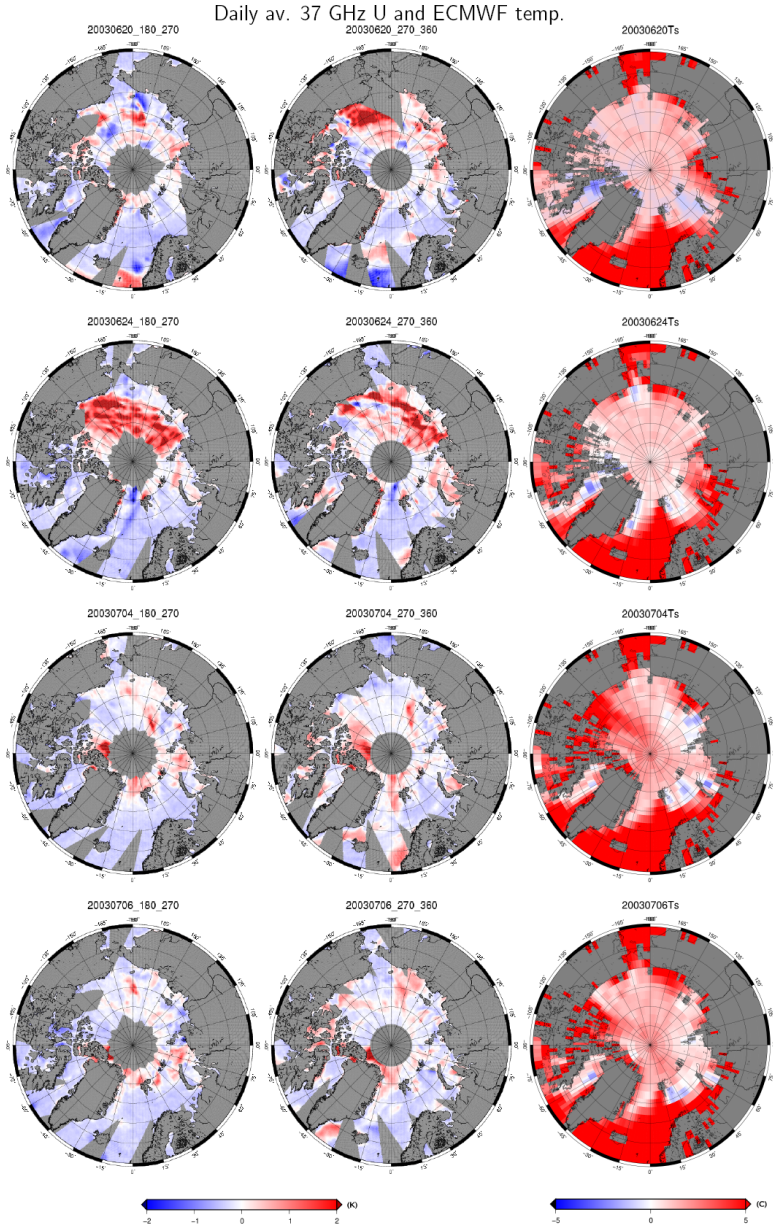
Figure 6.8: The 37 GHz U maps of $180°$ to $270°$ and $270°$ to $360°$ azimuth quadrants compared with ECMWF near surface air temperature map, June 20 to July 06, 2003.

6.2 Comparison with the ECMWF temperature data

During the analysis of the complete year of 2003 in last section, a higher signal at 37 GHz U was mainly observed during the early summer period (last week of June 2003). This indicates a possible relation between the polarimetric signal and the sea ice surface temperature. In order to gain more insight into the involved processes, we compare maps of EFMWF near-surface air temperatures with the 37 GHz U signal on a daily basis. As the first quadrant ($0°$ to $90°$) of the weekly averaged maps has a large gap around the pole in the data coverage (Figure 6.3), but the azimuth quadrants from $180°$ to $270°$ and from $270°$ to $360°$ are nearly completely covered by observations, we consider only the brightness temperature maps of the second and third quadrants. Figure 6.7 shows the daily averaged maps of 37 GHz U compared with ECMWF surface temperature map of $3^{r}d$ June 2003 in the first row. In the subsequent rows similar plots are shown for 5th June, 11th and 16th June. On 3rd June, the temperature is below freezing and the U signal is between ± 1 K. The first melting occurred during 11th to 16th June 2003, when the temperature rises above zero in most of the Arctic. However, only few areas within few hundred kilometres of the ice edge show a higher signal.

The largest closed area of high signal appears on the 20th of June (Figure 6.8, first row). The area of high signal decreases after 1st July, 2003 (Figure 6.8). The maximum is observed on the 24th June 2003 (second row of Figure 6.8). Later the signal reduces to below 1 K over most of the Arctic as shown in the third and fourth row of the Figure 6.8. Moreover, while the temperature rises above freezing in the whole Arctic, the high 37 GHz U signal has occurred at least once for every area covered by sea ice. In order to better understand the relation between the higher U and V signals and the temperature we selected three areas (100 x 100 km) across the Arctic, where the maximum signal has occurred in Figure 6.8, for preparing time series. Figure 6.9 shows the locations of these areas with center coordinates as Arc 1 (74.5 N, 158.7 W), Arc 2 (75.3 N, 174.0 W) and Arc 3 (77.0 N, 124.0 E). The first two Stokes components T_v and T_h has been extensively
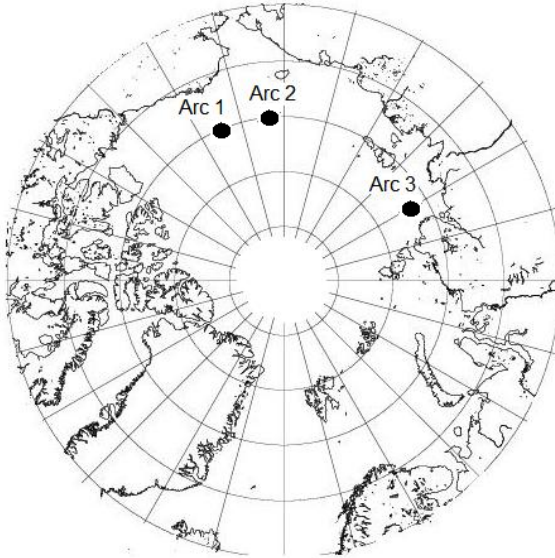
Figure 6.9: Map of the study area locations.

investigated with instruments such as AMSR-E and SSM/I for sea ice and are used to estimate the sea ice concentration as indicated in the earlier section. Figure 6.10 shows the time series of WindSat measured T_v and T_h over the study area Arc1.

The colors indicate the frequencies. The Gap in the time series is due to the unavailability of the data during October 2004. The decrease in the brightness temperature from June to August indicates the melting of the sea ice. The emissivity of the sea ice is around 0.9 and that of open water varies with frequency from 0.4 at 6.8 GHz to 0.7 at 37 GHz. As a consequence, the range of the seasonal cycle decreases with frequency from ∼150 K at 6.8 GHz to ∼80 K at 37 GHz.

The scale and variability of the T_v and T_h agrees well with the pervious studies made at similar frequencies (Spreen et al., 2007; Carsey, 1992). The melting of the sea ice can be verified from the ECMWF temperature time series of the first plot of Figure 6.11, which shows an increase in the surface temperature above melting during June.
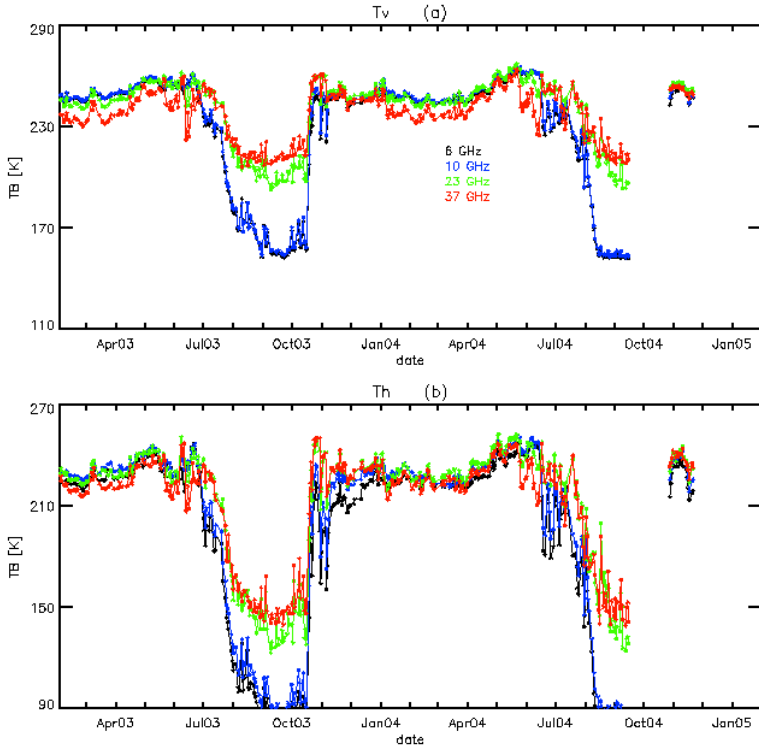
Figure 6.10: 6, 10, 23 and 37 GHz T_v (a) and T_h (b) time series from February 2003 to December 2004, for the location Arc1.

Similar was analysed for other study areas (Narvekar et al., 2008). Figure 6.11 compares the time series of daily minimum and maximum ECMWF surface air temperature (Figure 6.11a), SSM/I derived ice concentration (Figure 6.11b) and the 37 and 10.7 GHz U for the location Arc 1 for February 2003 to January 2005. The ECMWF temperature time series depicts the annual thermal cycle. Continuous melting sets on during June, with some isolated daytime melting events already in May. The first local maximum around 0.8 K in the 37 GHz U signal (Figure 6.11c) seems to mark the onset of melt. The absolute maximum of the season of over 2 K is reached end of June when the temperatures are continuously above freezing since more than one
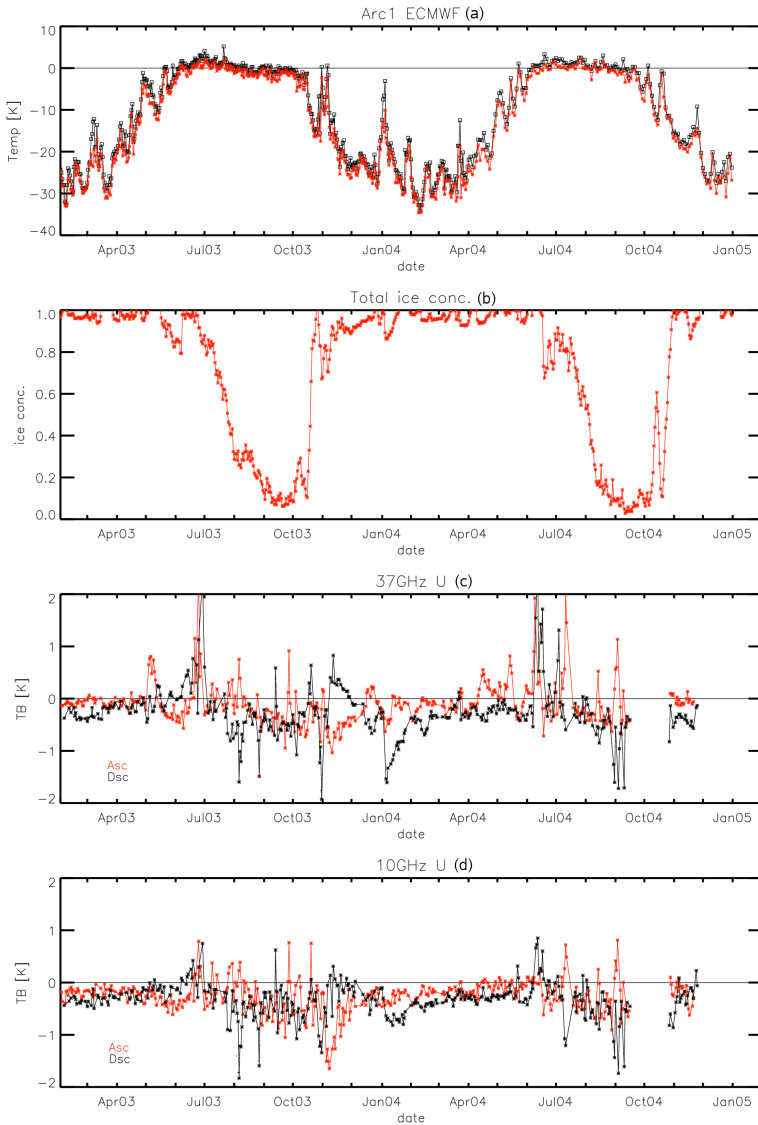
Figure 6.11: Time series of daily averaged 10.7 and 37 GHz U shown in (c) and (d) compared with time series of daily maximum (black) and minimum (red) ECMWF air surface temperatures in part (a) and sea ice concentration derived from SSM/I (b), from February 2003 to November 2004 for the study area location Arc 1. In (c) and (d) red means ascending and black descending orbits.
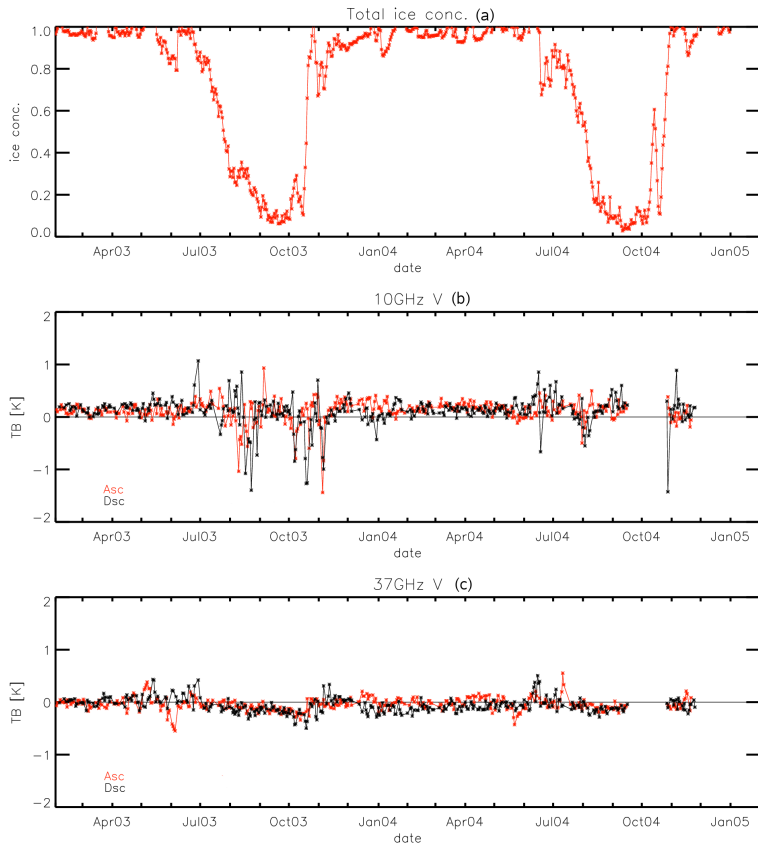
Figure 6.12: Time series of daily averaged 10.7 and 37 GHz V shown in (b) and (c) compared with time series of ice concentration derived from SSM/I (a), from February 2003 to November 2004 for the study area location Arc 1. In (b) and (c) redline means ascending and black descending orbits.

week, and when the ice concentration has reached about 80% during its summer decrease. Here we only consider the absolute values of the U signal. The sign is related to the azimuth direction of the anisotropic process generating the U signal. The azimuth dependency is not considered here. Obviously the higher U signal over sea ice relates to the processes that occur after melting of the surface sea ice starts. During the entire summer period the U signal is much more variable than during winter (Figure 6.11) with the highest signals occurring during June and during October to November. A sudden and isolated temperature rise in January 2004 from -30° C to nearly 0° C gives the clearest evidence of the relation between the temperature and the 37 GHz U signal, which increases from -0.3 K to -1.7 K. Although the peak in the ECMWF model near surface temperatures already reaches only about -2° C, it appears plausible to us that the peak at the same time in the 37 GHz U component is related to surface melting because in this data spares region easily model error can occur, and because it would be difficult to think of processes which occurs below melting temperatures generating processes at such large scales. The peak also allows estimating the relaxation time of the process: the 37 GHz U signal takes nearly one month to reduce to its original value. Presumably, this short event does not reach as deep as the penetration depth of 10.7 GHz because in the 10.7 GHz U channel the sudden temperature increase is not reflected. The U signal is more pronounced in the 37 GHz time series (Figure 6.11c) than at 10.7 GHz (Figure 6.11d). At 37 GHz it exceeds 2 K during the last week of June, when for 10.7 GHz it was below 1 K. As the 37 GHz radiation has a lower penetration depth than 10.7 GHz, the higher U signal must be produced by processes in the upper layers of the sea ice after melt onset. Figure 6.12 shows the comparison of the sea ice concentration with 10 and 37 GHz V. In the last section it was shown that the ice edge produces higher signal mainly in 10.7 GHz V. During the melting season, the ice concentration in Arc 1 reduces to nearly zero. The ice edge moves across the study area. In August and October the high 10.7 GHz V signal is clearly related to the ice edge. In contrast to 37 GHz U, the 37 GHz V signal is much lower (not exceeding 0.5 K, Figure 6.12c). Therefore, we presume that the processes generating the 10.7

V ice edge signal occurs not near the surface, but at the penetration depth of the 10.7 GHz signal. The relation of these processes to those generating the 10 V signal at the worldwide coastlines is unclear. The similar is observed for the other two areas, Arc 2 and Arc 3, see figures in (Narvekar et al., 2008).

6.3 Discussion and Conclusion

Analyses of the WindSat polarimetric U and V signals are carried out over the Arctic sea ice. In order to find out the period and location of higher polarimetric signals, maps of the year 2003 polarimetric U and V components are analysed and compared with the sea ice concentration maps derived from AMSR-E data. During most of the year, the 10.7 and 37 GHz U and V signals over sea ice is below 1 K. The exceptions are related to the melting period in summer and to the ice edge. All the higher signals in the U and V Stokes components occur during the melting period. This is in line with previous studies, e.g. by Markus and Dokken (2002), which reported a high variability of the sea ice emissivity also in the T_v and T_h Stokes components, reflecting the fact that the summer sea ice surface conditions are extremely variable in time as well as in space. In order to prove the dependency of the polarimetric signal on temperature, time series of ECMWF surface temperatures of the three regions of investigation were prepared. During the entire summer the U and V signal is more variable than during winter. The highest signal of up to 2 K occurs in the 37 GHz U channel. It can be very clearly related to the melting processes. The next highest signals are observed in the 10.7 GHz U and V channels. They reach up to about 1.7 K. One of the sources of the 10.7 GHz V signal is the ice edge. In contrast, the 10.7 GHz U signal seems to be related to melting processes of longer duration so that they reach the penetration depth of 10 GHz. The U signal at both 37 and 10.7 GHz suggests some geophysical anisotropic process during the melting season. They are present in both the top and the lower layers of Arctic sea ice. The reduced signal level at 10.7 GHz could be explained by attenuation of the signal by the uppermost sea ice layers. Although the

details are still unknown, the nonzero V signal seem to be related to the ice edge. The signal generating process could be similar to the one generating the V signals along the worldwide coastlines. A nonzero U signal requires quantities distributed anisotropically in azimuth within the footprint of the sensor. Currently we only can speculate on them. Plausible candidates could be unevenly distributed ice concentrations (e.g. the left half footprint completely ice covered, the right half open water), or microphysical properties influenced by vector quantities like wind or ice drift. However, in order to relate the higher polarimetric signature to the geophysical quantities of sea ice, more microphysical data of sea ice is required. It could be obtained from field campaigns on sea ice during early summer to shed more light on this topic.

7 Conclusions and Outlook

Fully polarimetric passive spaceborne measurements provided by Wind-Sat are investigated over land and snow and ice covered surfaces. The polarimetric studies carried out over the sea surface are extended over the land and snow ice areas in order to understand the third and fourth Stokes components, called U and V.

For the investigation of the U and V signals observed over land, large areas with know surface geophysical properties were selected, including the dense vegetation of the Amazon rainforest in Brazil, rangeland in Mongolia, the Taklamakan desert and the Heilonjiang agricultural area in China. The first two Stokes components T_v and T_h, were used as the reference channels. The Amazon rainforest area is an azimuthally isotropic target and, therefore, the U and V components should be close to 0 K. This area has also facilitated testing the bias associated with the fore and aft scan angles. Based on the analysis of all channels carried out over the entire scan angle range, the limited range of $-25°$ to $+25°$ in forward swath and from $140°$ to $155°$ in aft swath is selected. In addition, it was observed that the 18.7 GHz channel contains significant bias associated over the entire scan angle range. The observations at 18.7 GHz were therefore not considered.

Over the structured land covers such as desert and systematically oriented vegetated field, the U and V Stokes components are found to be a function of the orientation of the sand dunes and field rows, respectively. The magnitudes of these components were found to vary with the season for the agricultural area with changing vegetation. The signal becomes smaller after the harvesting period and disappears in winter for the bare soils. For the structured bare soils of periodic sand surfaces, the signal is related to the direction of the orientation of the sand dunes. For the bare soil with high topographic relief (area of

Mongolia) the U and V was near to 0 K except for the snow covered period during winter.

For the investigation of the U and V component over land ice, the Antarctic ice sheet was considered. The U and V signals depend on the snow deposition rate and other morphological properties. A second order harmonic sine function was fitted to the U and V observations. The first and second harmonic coefficients along with structural direction were estimated. The estimated coefficients and orientation angles from WindSat data at 10.7 GHz of February 2003 showed good agreement with the similar coefficients estimated using scatterometer dataset at 11 GHz of September 1996. The study shows for low frequencies (10.7 GHz observations) under winter conditions, that the high contribution of multiple volume scattering causes a high and regionally variable 10.7 GHz V signals as well as high backscattering coefficients, while under summer conditions, the surface scattering prevails, causing high U signals. For the 37 GHz channels that do not include contributions from deeper layers, the contrast between summer and winter observations was less pronounced.

Finally, an analysis is carried out over the Arctic in order to investigate the U and V components over sea ice. The results demonstrated that the lower frequency (10.7 GHz) shows almost isotropic response for most parts of the year. The signal observed is small than that observed over sea, land and snow surfaces. The 37 GHz U component has shown a high signal ($\sim$2 K) for a short period during the first melting event of Arctic ice. This signal was observed over large areas. However, the exact reason for the presence of the signal is not yet known. The ground experiment carried out by the Danish Meteorological Institute over the Arctic area is expected to shed light on the geophysical parameters responsible for the presence of the non-zero signal.

The thesis provides the potential of passive polarimetry for improvement of currently available approaches, utilized in various geophysical parameters retrievals using datasets from a single instrument. In the future, the polarimetric signatures over mixed land covers will be considered. Since the U and V component primarily depends on the surface geometric features, it will be possible to reduce the dependency of

the retrieval models on the ancillary sources for the parameters such as roughness and vegetation structure over land. Moreover, the new satellite mission SMOS will also observe the polarimetric channels at 1.4 GHz. This work will form the basis in the investigations of the new missions.

8 Acknowledgments

First of all, I would like to express my sincere thanks to my supervisor Dr. Georg Heygster for his continued interest, encouragement, support and valuable help when accomplishing this work. The thesis covers three vast topics; Passive polarimetry for the land, the Antarctic ice sheet and the Arctic sea ice. The first part of the work in this thesis has been completed at Hydrology and Remote Sensing Laboratory (HRSL), USDA, Maryland, United States. My special thanks goes to Dr. Thomas Jackson from HRSL for his support for maturing the research work at his laboratory in to some part my PhD thesis.

I am grateful to Dr. Li Li and Dr. Peter Gaiser from Naval Research Laboratory, Washington DC, United States for giving the access to the WindSat data sets, even after I changed my laboratory from HRSL to the Institute of Environmental Physics (IUP), University of Bremen, Germany. Here I am very much thankful to Prof. Justus Notholt for accepting me as his PhD student and for his continued support. I am thankful to Dr. Rasmus Tonboe from the Danish Meteorological Institute, Denmark for supporting the Arctic sea ice work within the framework of the Visiting Scientists Programme of the EUMETSAT Satellite Application Facility on Ocean and Sea Ice.

Finally I want to express my wholehearted thanks to all my colleagues from PHAROS group at IUP and HRSL,USDA united States for countless scientific discussions and for making my stay outside my home country very pleasant.

9 Bibliography

Bartalis, Z., Scipal, K., and Wagner, W., 2005: Azimuthal signature and scatterometer measurements over different land cover types in China. *ISPMSRS 2005, conference proceedings*, Beijing, China.

Bartalis, Z., Scipal, K., and Wagner, W., 2006: Azimuthal anisotropy of scatterometer measurements over land. *IEEE Trans. Geosci. Rem. Sens.*, **48**, 8, 2083–2093.

Bindlish, R., Jackson, T. J., Wood,E., Gao, H., Starks, P., Bosch, D. and Lakshmi, V., 2003: Soil moisture estimates from TRMM microwave imager observations over the south United States. *IEEE Trans. Geosci. Rem. Sens.*, **85**, 507–515.

Bingham, A., W.and Drinkwater, M., R., 2000: Recent changes in the microwave scattering properties of the Antarctica ice sheet. *IEEE Trans. Geosci. Rem. Sens.*, **38**, 1857–1870.

Brisset, L. and and Remy, 1996: Antarctic surface topography and kilometer scale features derived from ERS-1 satellite altimeter,*Annals of Glaciol.*, **23**, 374–381.

Calvet, J., Wigneron, J., Mougin, E., Kerr, Y., H. and Brito, L., 1994: Plant water content and temperature of the Amazon forest from satellite microwave radiometry, *IEEE Trans. Geosci. Rem. Sens.*, **32**, 2, 397–408.

Carsey, F. D. (Ed), 1992: *Microwave remote sensing of sea ice.* AGU Monograph, 68, Washington, D.C.: Am. Geophys. Union. 462 pp 71.

Comiso, J. C., 1983: Sea Ice Effective Microwave Emissivities From Satellite Passive Microwave and Infrared Observations. *J. Geophys. Res.*, **88**, C12, 7686–7704.

De Jeu, R. A., 2003: Retrieval of land surfave parameters using passive microwave remote sensing,*Ph.D. thesis, Faculty of Earth Science, Vrije Unversiteit*, Amsterdam, the Netherlands.

Flach, J., Partington., K., Ruiz, C., Jeansou, E. andDrinkwater, M.,
    2005: Inversion of the surface properties of ice sheets from satellite
    microwave data. *IEEE Trans. Geosci. Rem. Sens.*, **43**, 4, 743–752.

Fung, A. K., 1994: *Microwave Scattering and Emission Models and
    Their Applications.* Norwood, USA: Artech House.

Furukawa, T., Kamiyama, K. and Maeno, H., 1996: Snow surface fea-
    tures along the traverse route from the coast to Dome Fuji station,
    Queen Maud Land, Antarctica. *Proc. NIPR Symp. on Polar Mete-
    orol. Glaciol.*, **10**, 13–24.

Furukawa, T. and Young, N., 1997: Comparison of microwave backscat-
    ter measurements with observed roughness of the snow surface in
    east Queen Maud Land, Antarctica. *Proc. 3rd ERS Symp. on Space
    at the service of our environment*, ESA SP**414**, 803–807.

Gaiser, P., Germain, K., Twarog, E., Poe, G., Purdy, W., Richardson,
    D., Grossman, W., Jones, W., Spencer, D., Golba, G., Cleveland,
    J., Choy, L., Bevilacqua, R. and Chang, P., 2004: The WindSat
    spaceborne polarimetric microwave radiometer: sensor description
    and early orbit performance. *IEEE Trans. Geosci. Rem. Sens.*, **42**,
    2347–2361.

Goodwin, I., D., 1990: Snow accumulation and surface topography in
    the katabatic zone of eastern Wilkes Land, Antarctica.*Antacrt. Sci.*
    2(3),235–242.

Jackson, T., J., 1997: Soil moisture estimation using special satellite
    microwave/imager satellite data over grassland region. *Water re-
    source research*, **33**, 6, 1475–1484.

Jackson, T. J., Hurkmans,R., Hsu, A., and Cosh, M., 2004: Soil mois-
    ture algorithm using data from the advanced microwave scanning
    radiometer (AMSR-E) in Mongolia. *Italian Journal of Remote Sens-
    ing*, **30(31)**, 23–32.

Jackson, T. J., Bindlish, R., Gasiewski, A., Stankov, B., Klein, M.,
    Njoku, E., Bosch, D., Coleman, T., Laymon, C. and Starks, P.,
    2005: Polarimetric scanning radiometer C- and X-band microwave
    observations during SMEX03. *IEEE Trans. Geosci. Rem. Sens.*, **43**,
    11, 2418–2430.

Johnson, J. T. and Zhang, M., 1999: Theoretical study of the small

slope approximation for ocean polarimetric thermal emission. *IEEE Trans. Geosci. Rem. Sens.*, **37**, 2305–2316.

Johnson, J. T., 2002: Higher order emission model study of bi-sinusoidal surface brightness temperatures. *PIERS*, **37**, 79–99.

Jones, W. L., Park, J. D., Soisuvarn, S., Hong, L., Giaser, P. W. and Germain K. M., 2006: Deep-space calibration of the WindSat radiometer. *IEEE Trans. Geosci. Rem. Sens.*, **44**, 3, 476–495.

Kunkee, D. B. and Gasiewski, A. J., 1997: Simulation of passive microwave wind direction signatures over the ocean using anasymmetric-wave geometrical optics model. *Radio Sci.*, **32**, 59.

Kunzi, K. F., Fisher, A. D., and Stalien D. H., 1976: Snow and ice surface measured by the Niumbus-5 microwave spectrometer. *J. Geophys. Res.*, **81**, 4965–4980.

Kunzi, K. F., Patil, S., and Rott, H., 1977: Snow-cover parameters retrieved from Nimbus-7 scanning multichannel microwave radiometer (SMMR) data.*IEEE Trans. Geosci. Rem. Sens.*, **20**, 452–467.

Legresy, B., and Remy, F., 2000: Interferometry and altimetry at Dome C, Antarctica. *http://earth.esrin.esa.it/pub/*, online.

Liu, Q. and Weng, F., 2005: Vicarious calibration of the third and fourth Stokes parameters of WindSat measurements. *APPLIED OPTICS*, **44**, 34, 7403–7406.

Long, D. G., and Drinkwater, M. R., 2000: Azimuth variation in microwave scattermeter and radiometer data over Antarctica. *IEEE Trans. Geosci. Rem. Sens.*, **38**, 1810–1820.

Massom, R. A., Pook, M. J., Comiso, J. C., Adams, N., Turner, J., Lachlan-Cope, T., and Gibson, T. T., 2004: Precipitation over the Interior East Antarctic Ice Sheet Related to Midlatitude Blocking-High Activity. *Journal of Climate*,**17**, 1914–1928.

Meissner, T., and Wentz, F., 2002: Anupdated analysis of the ocean surface wind direction signal in passive microwave brightness temperatures. *IEEE Trans. Geosci. Rem. Sens.*, **40**, 6, 1230–1240.

Narvekar, P. S., Heygster, G., Jackson, T. J., Bindlish, R., and Li Li 2006: Azimuthal variations in polarimetric microwave measurements observed over Dome C, Antarctica. *Proceedings of SPIE*, **vol. 6410**.

Narvekar, P. S., Jackson, T., Bindlish, R., Li Li, Heygster, G. and

Gaiser, P., 2007: Observations of land surface passive polarimetry with the WindSat instrument. *IEEE Trans. Geosci. Rem. Sens.*, **45**, 7, 2019–2028.

Narvekar, P. S., Heygster, G. and Tonboe, R., 2007: Analysis of Wind-Sat measured passive fully polarimetric measurements over Arctic sea ice. *Tech. Rep., IUP, University of Bremen. Final Report for Danish Met. Insititute, Denmark.*

Nghiem, S. V., Veysoglu, M. E., Shin, R. T., Kong, J. A., O'Neill, K., and Lohanick, A., 1991: Polarimetric passive remote sensing of a periodic soil surface: microwave measurements and analysis. *J. Electromagn. Waves Appl.*, **5**, 9, 997–1005.

Njoku, E., Chan, T., Crosson, W. and Limaye, A., 2004: Evaluation of the AMSR-E data calibration over land. *Italian Journal of Remote Sensing*, **29**, 4, 19–37.

Naval Reasearch Laboratory, DC, U.S.A. Documnetation on WInd-Sat. *http://podaac.jpl.nasa.gov.*

Pham, H., Kim, E. J. andEngland, A. W., 2005: An calibration approach for microwave polarimetric radiometer. *IEEE Trans. Geosci. Rem. Sens.*, **43**, 11, 2443–2451.

Rotschky, G., Rack W., Dierking, W., and Oerter, H., 2006: Retrieving snowpack properties and accumulation estimation from a combination of SAR and scatterometer measurements.*IEEETGRS*, **44**, 943–956.

Sobjaerg, S., and Skou, N., 2003: Polarimetric signature from crop covered land surface measured by an L-band polarimetric radiometer.*Proc. IGRASS2003*, Toulouse, France.

Stephen, H. and Long D. G., 2005: Modeling microwave emissions of erg surfaces in the sahara Desert. *IEEE Trans. Geosci. Rem. Sens.*, **43**, 12, 2822–2830.

Surdyk, S. and Fily, M., 1995: Results of a stratified snow emissivity model based on the wave approach: Application to the Antarctic ice sheet. *J. Geophy. Research*, **100**, C5, 8837–8848.

Surdyk, S., 2002: Using microwave brightness temperature to detect short-tern surface air temperature changes in Antarctica: an analytical approach. *Rem. Sens. Envi.*, **80**, 256–271.

Tsang, L., Kong, J. A. and Shin, R. T., 1985: *Theory of Microwave Remote Sensing*. New York: Wiley.

Tsang, L., 1991: Polarimetric passive remote sensing of random discrete scatterers and rough surfaces. *J. Electromagn. Waves Appl.*, **5**, 1, 41–57.

Turner, J., Connolley, W., Leonard, S., Marshall, G., and Vaughan, D., 1999: Spatial and temporal variability of net snow accumulation over the Antarctica from ECMWF re-analysis project data. *Inter. Jour. Climatol.*,**19**, 697–724.

Twarog, E. M., Purdy, W. E., Gaiser, P. W., Cheung, K. H. and Kerlm, B. E., 2006: WindSat on-orbit warm load calibration.*IEEE Trans. Geosci. Rem. Sens.*, **44**, 3, 516–529.

Ulaby, F. T., Moore, R. K. and Fung, A. K., 1981: *Microwave Remote Sensing, Active and Passive. Volume I: Fundamentals and radiometry.* Norwood, USA: Artech House.

Ulaby, F. T., Moore, R. K. and Fung, A. K., 1982: *Microwave Remote Sensing, Active and Passive. Volume II: Theory.* Norwood, USA: Artech House.

Ulaby, F. T., Moore, R. K. and Fung, A. K., 1986: *Microwave Remote Sensing, Active and Passive. Volume III: From Theory to Applications.* 1990 edn., Norwood, USA: Artech House.

Van Den Broeke M., Van de wal,R. S., Wild, M., 1997: Representation of Antarctica kaabatic winds in a high-resolution GCM and a note on their climatic sensitivity. *American Meteorological Society.*

Yueh, S. H., 1997: Modeling of wind direction signals in polarimetric sea surface brightness temperatures. *IEEE Trans. Geosci. Rem. Sens.*, **35**, 1400–1418.

Yueh, S. H., Kwok, R.,Li, F. K., Nghiem, S. V., Wilson, W. J. and Kong, J. A., 1994: Polarimetric passive remote sensing of ocean wind vector. *Radio Sci.*, 799–814.

Yueh, S. H., Kwok, R. and Nghiem, S. V., 1994a: Polarimetric scattering and emission properties of targets with reflection symmetry. *Radio Sci.*, **29**, 6, 1409–1420.

Yueh, S. H., Wilson, W. J., Dinardo, S. J. and Hsiao, S. V., 2006: Polarimetric microwave wind radiometer model function and retrieval

testing for WindSat.*IEEE Trans. Geosci. Rem. Sens.*, **44**, 3, 584–596.